INSTITUTO POLITÉCNICO DE BRAGANÇA Escola Superior de Tecnologia e Gestão

UNIVERSIDADE TECNOLÓGICA FEDERAL DO PARANÁ

Phase change materials for thermal storage in solar dehydrators

Nickolas Giacomitti

Dissertation presented to the Double Degree Program between the Federal Technological University of Paraná and the Polytechnic Institute of Bragança, as a requirement for obtaining the title of Master in Mechanical Engineering.

Supervisors:

Doctor Luís Frölén Ribeiro

Doctor Cláudio Tavares da Silva

Bragança

2024

This page has been intentionally left blank.

INSTITUTO POLITÉCNICO DE BRAGANÇA Escola Superior de Tecnologia e Gestão

UNIVERSIDADE TECNOLÓGICA FEDERAL DO PARANÁ

Phase change materials for thermal storage in solar dehydrators

Nickolas Giacomitti

Dissertation presented to the Double Degree Program between the Federal Technological University of Paraná and the Polytechnic Institute of Bragança, as a requirement for obtaining the title of Master in Mechanical Engineering.

Supervisors:

Doctor Luís Frölén Ribeiro

Doctor Cláudio Tavares da Silva

Bragança

2024

This page has been intentionally left blank.

Dedication

I dedicate the following work for:

To my beloved family, who remained steadfast in their support despite the distance that separates us. Your unwavering encouragement and belief in my dreams have been my guiding light throughout this journey. I carry your love with me every step of the way.

To my cherished girlfriend, whose courage and sacrifice exemplify true partnership and unwavering commitment. Your willingness to embark on this adventure with me, leaving behind everything familiar, is a testament to our bond and shared aspirations.

To my dear friends, whose invaluable assistance and encouragement have been instrumental in the realization of this thesis. Your steadfast support and camaraderie have infused this journey with joy and camaraderie, reminding me that no challenge is insurmountable with friends by my side.

This work is dedicated to you, my pillars of strength, with heartfelt gratitude and love.

This page has been intentionally left blank.

Acknowledgment

I would like to extend my sincere gratitude to Dr. Luís Frölén Ribeiro for his invaluable guidance and expertise throughout this research. His insights into thermal storage was fundamental to the development and completion of this thesis.

I am also deeply thankful to Dr. Cláudio Tavares da Silva for his technical knowledge and constructive feedback, which were essential in refining and enhancing the analysis. His support greatly contributed to the quality of this work.

To Luis Mesquita, who assisted in acquiring the optimal mesh configuration for accurate simulations.

To Paulo Bruno provided guidance in navigating the CFD ANSYS software in early simulation stages and further analysis.

Additionally, Matheus Alves contributed to the organization of the thesis as well as the validation and interpretation of the results.

Felipe Stein provided invaluable assistance with the interpretation and calculations of certain equations, which I encountered some difficulties in managing.

This page has been intentionally left blank.

Abstract

This thesis examines the feasibility of Phase Change Material (PCM)-based Thermal Energy Storage (TES) systems designed for use in solar thermal collectors for air heating and food dehydration applications. Through a combination of analytical methods and numerical simulations, the study evaluates the thermal behavior of selected PCM under diverse environmental conditions, focusing on their liquefaction and solidification properties. The simulations were conducted in Ansys Fluent for both summer and winter conditions, using its integrated solar calculator to simulate solar radiation and energy output. Although the solar calculator required correction to match expected solar irradiance, the results aligned with anticipated outcomes. The findings highlight the efficacy of different PCM in regulating temperature and storing thermal energy during off-sun hours in solar collector applications. Key results demonstrate that while Sodium Sulfate Decahydrate (SSD) performs well for winter applications, requiring 90 kg of material at a cost of €5,42 per m^2 of solar collector and yielding a 4,84°C temperature difference between the collector inlet and outlet in peak winter, Iron (III) Sulfate Heptahydrate (ISH) shows stability and efficiency in summer conditions. The ISH requires 112 kg of material, costs €17,38, and achieves a 13,1°C temperature difference between inlet and outlet for peak summer. Both materials exhibit the lowest cost per m^2 for capturing direct solar irradiance, with SSD demonstrating a phase-change temperature suitable for winter conditions and ISH performing optimally in summer conditions.

Keywords: Thermal Energy Storage, Phase Change Materials, Solar Thermal Collectors, Energy Efficiency, Sodium Sulfate Decahydrate, Iron (III) Sulfate Heptahydrate.

This page has been intentionally left blank.

Resumo

Esta tese examina a viabilidade de sistemas de armazenamento de energia térmica (TES) baseados em materiais de troca de fase (PCM), projetados para uso em coletores solares térmicos para aplicações de aquecimento de ar e desidratação de alimentos. Por meio de uma combinação de métodos analíticos e simulações numéricas, o estudo avalia o comportamento térmico dos PCMs selecionados, com foco em suas propriedades de liquefação e solidificação. As simulações foram realizadas no Ansys Fluen para condições de verão e inverno, utilizando seu calculador solar para simular a radiação solar. Embora o calculador solar exigisse correção para igualar a irradiância solar esperada, os resultados corresponderam aos antecipados. Os achados destacam a eficácia dos diferentes PCMs na regulação da temperatura e no armazenamento de energia térmica durante as horas sem sol em aplicações de coletores solares. Enquanto o sulfato de sódio decaidratado (SSD) apresenta um bom desempenho para aplicações de inverno, exigindo 90 kg de material a um custo de €5,42 e fornecendo uma diferença de temperatura de 4,84°C entre a entrada e a saída do coletor em condições de inverno, o sulfato de ferro (III) heptaidratado (ISH) mostra estabilidade e eficiência nas condições de verão. O ISH requer 112 kg de material, custa €17,38 e alcança uma diferença de temperatura de 13,1°C entre a entrada e a saída do coletor em condições de verão.

Palavras-chave: Armazenamento de Energia Térmica, Materiais de Mudança de Fase, Coletores Solares Térmicos, Eficiência Energética, Sulfato de Sódio Decaidratado, Sulfato de Ferro (III) Heptaidratado.

This page has been intentionally left blank.

Contents

List of Figures

List of Tables

This page has been intentionally left blank.

Acronyms

CFD Computational Fluid Dynamics.

IPB Instituto Politécnico de Bragança.

ISH Iron (III) Sulfate Heptahydrate.

LHS Latent Heat Storage.

PCM Phase Change Material.

PCMs Phase Change Materials.

PVGIS Photovoltaic Geographical Information System.

SC Solar Calculator.

SHS Sensible Heat Storage.

SSD Sodium Sulfate Decahydrate.

STB Solar Thermal Battery.

STP Sodium Thiosulfate Pentahydrate.

TES Thermal Energy Storage.

This page has been intentionally left blank.

Chapter 1

Introduction

Thermal energy storage (TES) systems have emerged as a critical area of research due to their potential to enhance energy efficiency and decrease reliance on conventional energy sources. The integration of Phase Change Materials (PCMs) into TES systems presents a promising approach for effectively storing and utilizing thermal energy, particularly in solar thermal applications.

This thesis focuses on the development of TES systems utilizing PCMs, emphasizing their role in solar thermal energy utilization. Mechanical engineering plays a vital role in advancing energy systems that efficiently manage the storage and release of thermal energy. By coupling TES systems with PCMs, this research addresses significant challenges related to solar thermal energy storage. The study employs Computational Fluid Dynamics (CFD) modeling in Ansys software to simulate the behavior of PCM-based TES systems.

The objective of this work is to propose a TES solution utilizing PCMs designed to meet the requirements of a solar thermal food dryer. This research aims to provide heat supply during periods without solar incidence and minimize drying times, contributing to the development of TES systems powered by renewable sources and promoting sustainable practices in relevant sectors.

To achieve these goals, the study evaluates the performance of three different PCMs under summer and winter conditions.

The overarching objective of this thesis is to develop an TES system utilizing PCMs to store solar thermal energy for air-heating applications. Additionally, the following specific goals are set:

- identify various PCMs with optimal characteristics for solar energy storage;
- develop a numerical simulation model in Ansys Fluent to predict the thermal performance of selected PCMs in summer and winter conditions;
- assess the impact of different PCMs on temperature regulation and energy storage during off-sun hours;
- propose potential improvements for the system based on simulation results.

This study focuses on three selected PCMs: SSD, Sodium Thiosulfate Pentahydrate (STP), and ISH. These materials were selected based on their high latent heat capacity exceeding 200 $kJ/(kg \cdot K)$, cost-effectiveness where the price per kilogram of the selected PCM is less than 1 euro, and melting temperatures within the range of 40°C.

Numerical simulations were conducted using ANSYS Fluent to evaluate the thermal behavior of the PCMs under solar energy conditions. The air inlet, outlet temperatures and phase change behaviors of PCM were analyzed under different environmental conditions, with the simulation parameters adjusted for seasonal variations.

The simulation results demonstrated the effectiveness of the selected PCMs in regulating temperature and storing thermal energy, particularly in summer conditions. Among the materials, ISH showed the most promising results for summer applications due to its high phase-change temperature and energy capacity. Conversely, SSD was found to be more suitable for intermediate seasonal applications, such as autumn or spring although the simulations was conduced in peak winter conditions, the SSD demonstrated suboptimal results for this conditions, but it can be too used in winter conditions.

This thesis is organized into five main chapters.

Chapter 1 provides an introduction to the study, outlining the framework, objectives, materials, methods, and the overall structure of the thesis. It sets the foundation for the

research by defining work and presenting the key goals to be presented throughout the research.

Chapter 2 depicts the literature review, focusing on the use of PCM in TES systems, solar thermal energy applications, and previous studies related to the development of solar collectors. This chapter also establishes the theoretical background and highlights the state of the art in the field of TES technologies.

Chapter 3 details the materials and methods used in the study, including the selection criteria for PCM, numerical modeling, and simulation setups. This section elaborates on the technical approach and methodology adopted to achieve the research objectives.

Chapter 4 discusses the results obtained from the simulations, with a focus on temperature evolution, energy efficiency, and phase-change behavior of the PCMs. The chapter interprets the results and provides an analysis of the system's performance under different conditions.

Chapter 5 concludes the thesis, summarizing key findings, suggesting areas for further research, and providing recommendations for future developments in TES systems using PCM. It synthesizes the outcomes of the research and offers insights for advancing the field.

This page has been intentionally left blank.

Chapter 2

Theoretical Framework

This chapter presents the essential theoretical foundations required to understand the research conducted in this study.

2.1 State-of-the-art

The field of mechanical engineering has seen significant advancements in the realm of TES systems, particularly in the context of drying chambers. The efficiency of these systems is paramount, and recent studies have shed light on the comparative performance of different types of TES.

The energy used for food drying comes from various sources, including fossil fuels, natural gas, and solar energy. The use of solar energy for food drying has gained popularity due to the rapid depletion of natural fuel resources, increasing fossil fuel costs, and growing concerns about environmental damage [1], [2].

Indirect solar drying, where ambient air is heated by a solar collector before entering a drying chamber to remove moisture from food placed on rack shelves, has been proposed by various researchers [2]–[4]. Figure 2.1 presents an example of an indirect solar food dryer, where the flat plate collector is utilized to capture solar thermal energy and transfer it to the air flowing through the system. The temperature increase of the air within the collector, compared to the ambient air, induces a pressure difference that generates airflow,

driving the air through the dryer [5]. The drying camera is responsible for holding the product that need to be dried. This type of solar dryer offers advantages such as improved product quality and reduced drying time. However, significant improvements are needed to achieve uniform drying. Non-uniform drying can lead to microbial risks and substantial variations in the quality of the dried food, primarily due to the uneven distribution of airflow and temperature within indirect solar dryers. Although many design optimizations have been proposed to address this issue, they have not yet been fully developed to predict airflow and transient heat transfer phenomena [6].

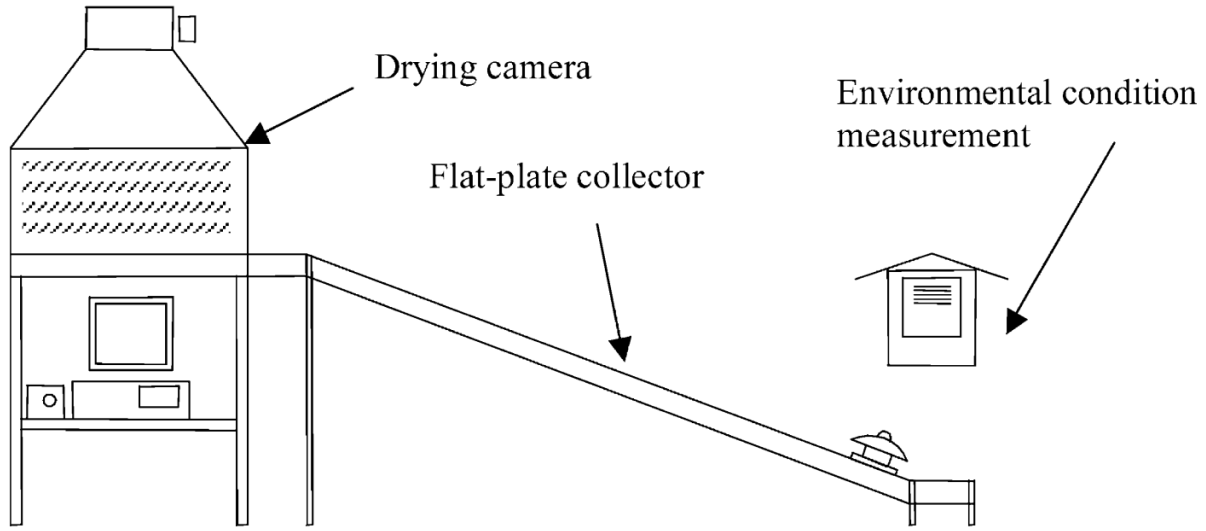

Figure 2.1: Indirect solar drying [5]

The optimization of drying processes through the integration of TES systems within solar thermal dryers has received considerable attention due to its potential to enhance drying efficiency and reduce overall drying times. In a comparative study conducted by [7], the drying time varied significantly across different drying configurations. Specifically, the drying times for systems without a drying chamber, with a drying chamber lacking thermal storage, utilizing Sensible Heat Storage (SHS), and employing Latent Heat Storage (LHS) were 17 hours, 12 hours, 11 hours, and 8 hours, respectively. Notably, the use of LHS resulted in a drying time 1.5 times faster than systems without any heat storage and 1.375 times faster than those employing SHS. This improvement translated to a substantial 33%

decrease in drying time, underscoring the efficacy of LHS in optimizing dryer performance.

[8] conducted a study to assess the potential of a paraffin wax-based TES system. The primary function of this system was to harness solar energy during periods of sunlight and subsequently release it during hours devoid of sunlight. The solar energy accumulator, a key component of the system, was filled with 60 kg of paraffin. The results of the study were promising, with the accumulator effectively maintaining the temperature of the drying cabinet at a level 4–16 ^{o}C above the ambient temperature during the non-sunny hours of operation.

Further insights from [9] provided detailed characteristics of LHS and SHS systems. The LHS system demonstrated superior energy storage capabilities, with a cumulative energy absorption capacity of 2,66 kWh, surpassing the SHS system. However, the SHS system exhibited faster charging times, particularly notable for medium energy storage capacities. Despite the efficiency of LHS, the charging time was approximately 10,7% higher compared to SHS due to the higher thermal storage of the latent material.

Moreover, thermal conductivity played a crucial role in determining heat transfer rates [9]. The SHS system exhibited better heat transfer rates owing to the higher thermal conductivity of concrete spheres, leading to a more favorable thermal gradient compared to LHS under similar flow rate conditions[9].

In addition, the mass flow rate was found to significantly affect the charging time and heat transfer rate in both storage systems, with high instantaneous energy absorption rate and high heat transfer rates obtained at higher mass flow rate conditions, highlighting the significance of flow dynamics in optimizing system performance [9].

[10] investigated a solar dryer with an integrated solar collector and a PCM-based energy storage unit. The unit, filled with 14 kg of paraffin wax in 100 copper tubes, stored thermal energy during sunny hours for use after sunset. This system maintained the drying cabinet temperature 20 ^{o}C above ambient for about 2 hours, reducing electrical consumption by 40–70%. The solar collector and accumulator achieved maximum thermal efficiencies of 62% and 21%.

Several studies have contributed valuable insights into the practical applications of

TES in solar thermal dryers. For instance, [11] demonstrated the efficacy of PCM in extending drying times, using 50 kg pf PCM they achieve to extend the working period of the dryer by 5-6 hours. While [12] highlighted the role of TES in reducing drying time compared to conventional methods, the research achieved a 7 hours increase in the dryer functioning period and, this increase in the equipment function period resulted in 37,50% and 64,29% decrease in drying time as compared to heat pump drying and traditional open-sun drying.

Similarly, various studies have explored TES configurations and materials to enhance drying efficiency in solar dryers across different environmental conditions. [13] investigated an indirect solar dryer using paraffin wax as a PCM to store thermal energy. Their setup used 18 kg of PCM integrated into the dryer and demonstrated a consistent release of heat, which stabilized drying temperatures during off-sun hours, reducing total drying time by about 30% for fruits and vegetables in moderate climates. [14] focused on a solar fish dryer that utilized 12 kg of PCM (specifically, paraffin wax) and found it maintained a stable drying temperature between 45°C and 50°C. This approach improved the drying process's uniformity and quality, resulting in a significant reduction in drying time and energy dependency.

[15] examined a combined direct and indirect solar dryer with 10 kg of sensible heat storage material, specifically gravel, used for camel meat drying in the challenging Saharan environment. Their results demonstrated that the dryer could maintain temperatures up to 70°C, which is optimal for meat drying, while improving energy efficiency and reducing microbial risks in extreme climates. Finally, [16] analyzed a packed bed TES system for a solar dryer, using 15 kg of pebbles as the storage medium. The study showed that the dryer could retain temperatures between 50°C and 60°C during off-sun hours, effectively extending the operational period and improving the dryer's adaptability to variable sunlight conditions.

2.2 Background

2.2.1 Thermal Energy Storage

TES is categorized into SHS, LHS and Chemical Heat Storage [17]. However, TES systems utilizing PCMs have garnered significant attention among researchers due to their numerous advantages [18], [19]. These advantages include:

- Heat storage at a constant temperature corresponding to the phase transition temperature of the PCM.
- Significantly higher energy storage capacity, ranging from 5 to 14 times more energy per unit volume compared to sensible heat materials such as water and rock.
- The versatility of LHS, which can be achieved through various phase transformations including solid-liquid, liquid-gas, solid-gas, and solid-solid transitions.

The present study will focus on 2 of those TES methods: sensible heat storage and latent heat storage focused on PCM for Solar Thermal Battery (STB) applications.

Sensible Heat Storage

Sensible heat storage: represents the most straightforward and uncomplicated form of heat storage technology. In this method, the material retains thermal energy in a manner where it does not undergo a phase change within a defined temperature range. For instance, when heat is applied to water, it can either raise its temperature or cause it to change its phase. Therefore, the energy required solely to elevate its temperature without inducing a phase change is referred to as the sensible heat of the water.

The sensible thermal energy inside any material can be given by the equation 2.1:
2.1:

$$Q = mc_p\Delta T \tag{2.1}$$

Where Q (kJ) is the heat stored in the material, m (kg) is the total mass of the material that will hold the thermal energy, c_p (kJ/kg K) is the material specific heat and

ΔT (K) is the temperature variation without any phase change. The amount of sensible heat in a material is determined by its mass and specific heat [20].

Nearly all materials exhibit distinct specific heat values during phase transitions, resulting in differences in thermal energy storage between phases. Consequently, the amount of thermal energy stored over a given temperature variation in the solid phase differs from the energy stored over the same temperature range when the material is in its liquid or gaseous phase.

Latent Heat Storage

LHS operates by absorbing or releasing heat during a phase change of a storage material, transitioning between solid to liquid or liquid to gas, and vice versa. The storage capacity of an LHS system utilizing a PCM medium is determined by the amount of storage material, the endothermic heat of reaction, and the extent of conversion. LHS systems offer several advantages over SHS systems, with the most significant being higher energy density per unit mass and volume. Among thermal heat storage techniques, latent heat thermal energy storage is particularly appealing due to its capability to provide high energy storage density. It also presents the ability to store heat at a constant temperature corresponding to the phase transition temperature of the PCM [21]. The amount of thermal energy that is stored in the phase transition of certain PCM material is given by the equation 2.2:

$$Q = a_r m \Delta h_r \tag{2.2}$$

Where Q (kJ) is the heat stored in the material, a_m is the total fraction of the material that will change phase, m (kg) is the total mass of the material that will hold the thermal energy, Δh_r (kJ/kg) is the enthalpy of fusion of the material.

2.2.2 Phase change materials

A PCM has the capability to absorb, store, and release thermal energy almost isothermally at its phase change temperature. Depending on the desired application, mode of operation, and phase change temperature, a thermal battery using PCM can function either as a heat source or a heat sink. The selection of a suitable PCM for a specific application depends on factors such as its phase change temperature, system size, external operating temperatures, and cost considerations [22].

Extensive research has been conducted on incorporating PCMs into building systems, focusing on two main schemes: passive and active systems. In passive systems, the PCM serves as an inconspicuous and uncontrolled thermal buffer to manage high transient thermal loads on the building envelope. In contrast, in active systems, the PCM is integrated with a heat pump or similar mechanical device, allowing controlled absorption or release of heat according to the needs of the operators. The successful implementation of passive and active PCM systems is based on the selection of a PCM with an appropriate phase change temperature tailored to the specific requirements of the application [21], [22].

Comparing latent and sensible heat storage reveals that latent heat storage offers significantly higher storage densities, typically ranging from 5 to 10 times greater. Furthermore, the volume required for storage of PCM is approximately half that of water [23], [24].

Latent heat storage is applicable across a broad temperature spectrum due to the availability of numerous PCMs that melt within specified heat of fusion ranges. The selection of a PCM for designing thermal storage systems necessitates achieving desirable thermophysical, kinetic, and chemical properties [23], [25], [26].

- Thermo-physical Properties

    1. Melting temperature in the desired operating temperature range;
    2. High latent heat of fusion per unit volume so that the required volume of the container to store a given amount of energy is lower;

3. High specific heat to provide for additional significant sensible heat storage;
4. High thermal conductivity of both solid and liquid phases to assist the charging and discharging of energy of the storage systems;
5. Small volume changes on phase transformation and small vapor pressure at operating temperatures to reduce the containment problem;
6. Congruent melting of the PCM for a constant storage capacity of the material with each freezing/melting cycle.

- Kinetic Properties

1. High nucleation rate to avoid super cooling of the liquid phase;
2. High rate of crystal growth, so that the system can meet demands of heat recovery from the storage system.

- Chemical Properties

1. Chemical stability;
2. Complete reversible solidification/melting cycle.
3. No degradation after a large number of solidification/melting cycles;
4. Non-corrosiveness to the construction materials;
5. Non-toxic, non-flammable, and non-explosive materials for safety.

Other characteristics that are also important are the price of the PCM and the market availability of the desired material.

Groups

PCMs can be categorized into three distinct groups, as illustrated in Figure 2.2, with descriptions provided for each group below.

- **Organic**

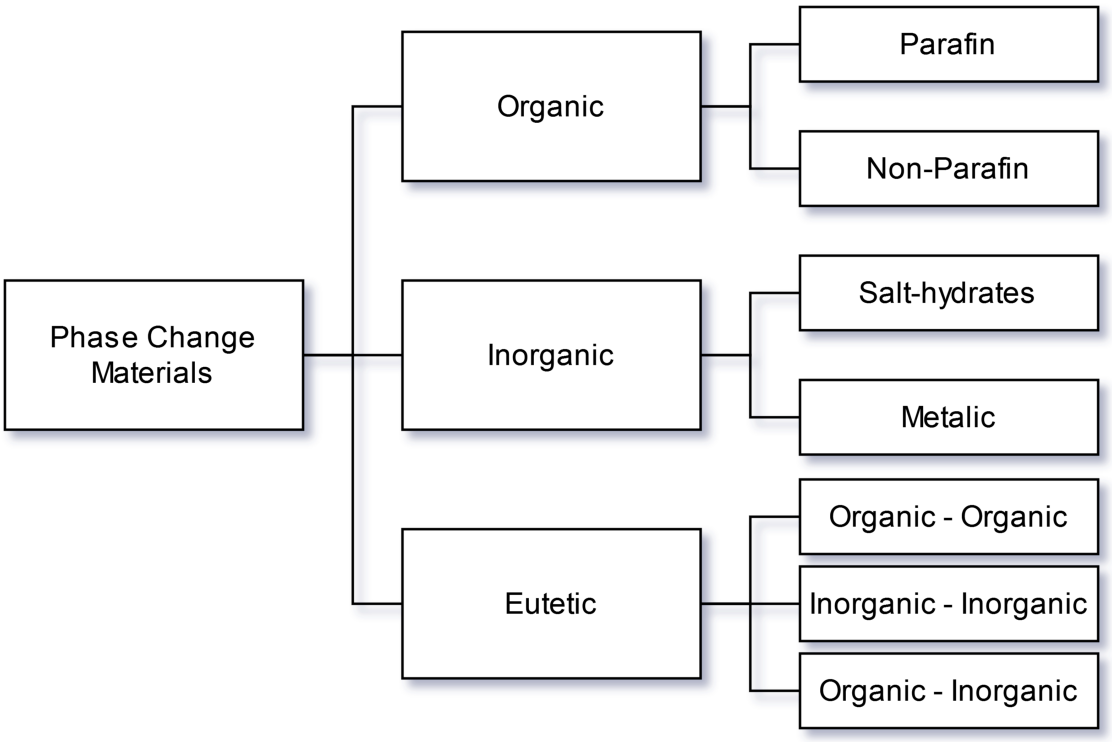

Figure 2.2: Segmentation of the phase change materials.

Paraffin wax stands out as the most commonly utilized commercial organic heat storage PCM, readily accessible from numerous manufacturers, albeit typically more costly than salt hydrates [26], [27]. It primarily comprises straight-chain hydrocarbons with melting temperatures ranging from 23 to 67 °C [28].

Advantages: Paraffin waxes exhibit several advantages, including their tendency to remain homogeneous without segregating and their chemical stability [21]. Commercial-grade paraffin wax maintains stable properties even after 1500 cycles of use [29]. These waxes also demonstrate no significant degradation in thermal properties after repeated melting and freezing cycles. They possess high heats of fusion and do not require nucleating agents to prevent supercooling [25], [27]. Paraffin waxes are safe, non-reactive, and compatible with all metal containers, making them easily integrable into heat storage systems [27]. However, caution is advised when using plastic containers, as paraffins can

infiltrate and soften certain plastics [27].

Disadvantages: Despite their advantages, paraffin waxes have limitations, notably low thermal conductivity in their solid state, which poses challenges when rapid heat transfer rates are required during the freezing cycle [21]. They also undergo significant volume changes between their solid and liquid states, presenting difficulties in container design [24], [27]. Paraffins generally lack sharp, well-defined melting points unlike Salt Hydrates, which can affect their heat storage capacity [27]. Additionally, paraffin waxes are flammable, although this risk can be mitigated by using appropriate containers [24].

Non-paraffin organic materials represent the largest category of PCMs, characterized by diverse and varied properties unique to each material unlike paraffins, which exhibit similar properties. However, these organic PCMs are flammable and should be protected from high temperatures, flames, or oxidizing agents. [27], [28] conducted comprehensive research of organic materials, identifying numerous esters, fatty acids, alcohols, and glycols suitable for energy storage applications.

- **Inorganic**

Inorganic PCMs are classified into two types: salt hydrates and metallic hydrates. Salt hydrates consist of elements from the inorganic salt family (oxides, nitrates, and halides) combined with water molecules in specific ratios [30]. These salts undergo dehydration during the phase transformation process [31]. Depending on their phase transition behavior, salt hydrates can be categorized into three types: incongruent behavior, semi-congruent behavior, and salt hydrates with congruent melting behavior. There are numerous salt hydrates that can serve as potential choices for PCMs due to their diverse properties [32].

Advantages: Salt hydrates are attractive for heat storage applications due to their low cost and widespread availability [27]. Two commonly used and inexpensive salt hydrates are $CaCl_2.6H_2O$ and $Na_2SO_4.10H_2O$ (Glaubers salt) [27]. They exhibit sharp melting points and high thermal conductivity compared to other heat storage PCMs, facilitating efficient heat transfer in and out of the storage unit. Salt hydrates also have

a high heat of fusion, allowing for smaller storage system sizes. Additionally, they experience lower volume changes compared to other PCMs, simplifying container design [21].

Disadvantages: One drawback of salt hydrates is segregation, where other hydrates or dehydrated salts settle out and reduce the active storage volume. $Na_2SO_4.10H_2O$ demonstrate a significant decrease (over 73%) in the heat of fusion after 1000 solidification / melting cycles [28]. This issue can be partially addressed by using gelled or thickened mixtures [27], although this approach can negatively impact heat storage performance and does not completely prevent degradation over time [28]. Salt hydrates are prone to supercooling because they do not spontaneously crystallize at freezing points, but this can be mitigated by using nucleating materials to initiate crystal growth in the storage media [27]. $CaCl_2.6H_2O$ presented material degradation after only two cycles when the test sample was not hermetically sealed, emphasizing the need for proper container design to prevent moisture loss [28]. Salt hydrates also have a tendency to cause corrosion in metal containers commonly used in thermal storage systems [28], underscoring the importance of compatibility testing between PCM and container materials prior to use [21].

- **Eutectic**

A eutectic refers to the minimum melting composition of two or more components, where each component melts and freezes congruently, resulting in the formation of a mixed crystal structure during crystallization [27]. Eutectics typically undergo melting and freezing without segregation because they solidify into an intimate mixture of crystals, minimizing the chance of component separation. When melted, both components liquefy simultaneously, further reducing the likelihood of separation [21].

Super-cooling

Supercooling occurs when the formation of stable solid nuclei is impeded by a fixed free energy barrier, preventing nucleation at the critical radius (R_{cr}). This results in a degree of subcooling (T_{sc}), defined as $T_{sc} = T_m - T_s$, where T_m is the melting temperature and T_s

is the solidification or freezing temperature. The level of supercooling can be quantified by the equation $T_{sc} = \frac{3}{4}[\gamma_o T_m/(\rho^s \Delta H R_{cr})]$, where γ_o is the surface free energy per unit area, ρ_s is the density of the solid, and ΔH is the enthalpy of fusion [33]. Supercooling occurs when a large T_{sc} is achieved, allowing for spontaneous homogeneous nucleation with stable nuclei. Controlling the degree of supercooling is crucial for latent heat energy storage, as it affects the quality of released heat and the utilization of thermal energy [34].

Advantages of Supercooling: Utilizing supercooling can enhance the efficiency of latent heat storage applications, as indicated by numerical simulations [35]. Longer storage periods can increase efficiency, with operating temperature also playing a role [36], [37]. Certain PCMs can remain in a supercooled state below their melting temperature, providing potential benefits in specific applications [38].

Disadvantages of Supercooling: The freezing temperature may not align with the desired temperature range controlled by a system, potentially increasing energy consumption [39]. There is a risk of PCM not freezing completely, impacting heat release and system performance, particularly if the heat transfer fluid temperature is close to the freezing point [39]. Randomness and unpredictability of supercooling make it difficult to control LHS systems, limiting their widespread applicability [39]. Significant changes in PCM density during phase change can cause container ruptures or deformations, posing operational risks [39]. Supercooling affects temperature margins within thermal systems, potentially leading to critical design issues and system failures [39]. For temperature control applications, supercooling necessitates operating the system at lower temperatures, increasing design complexity and inefficiency [39]. Small volumes exhibit higher degrees of supercooling compared to bulk PCMs, impacting crystal growth and system performance [39].

To mitigate the challenges associated with supercooling, various techniques have been explored, including the use of nucleating agents, encapsulation, and emulsion techniques [40], [41].

Encapsulation Methods

Encapsulation can be broadly categorized into two methods: macroencapsulation and microencapsulation.

Macroencapsulation involves packaging PCM in larger containers such as tubes, pouches, spheres, or panels, which can serve as heat exchangers or be integrated into building products [42]. However, traditional macroencapsulation methods faced challenges due to poor heat transfer rates caused by PCM freezing on heat exchanger surfaces, which is attributed to the low thermal conductivity of PCMs [43]. Despite these difficulties, macroencapsulation of $CaCl_2.6H_2O$ in plastic and metal containers showed promise for heating systems using air as the heat transfer medium [43].

Microencapsulation, developed in the late 1970s, involves packaging micronized PCM materials in capsules ranging from less than 1 mm to over 300 mm using a variety of wall materials such as natural or synthetic polymers [42]. Microencapsulation offers several advantages, including increased heat transfer area, reduced PCM reactivity to the external environment, and controlled volume changes during phase change [42]. This technique allows PCM to be economically incorporated into conventional construction materials and textile fibers, offering enhanced thermal protection in various environments [42].

2.2.3 Solar radiation

Global solar radiation is the total solar energy received at the Earth's surface, comprising two key components: direct beam radiation and diffuse radiation. Direct beam radiation refers to solar energy that travels through the atmosphere and reaches the surface without significant scattering or absorption. In contrast, diffuse radiation is the portion of sunlight scattered or reflected by atmospheric particles such as air molecules, water vapor, clouds, dust, and pollutants. The sum of these components forms global radiation, with atmospheric conditions playing a significant role in modulating the levels of each. On clear days, direct beam radiation predominates, while on cloudy or polluted days,

diffuse radiation becomes more substantial. These variations in atmospheric conditions can reduce direct beam radiation by up to 100%, yet diffuse radiation may still contribute to the total global radiation reaching the surface [44].

Chapter 3

Material and methods

This chapter will detail the methods employed to investigate the utilization of PCMs for use in STB applications.

3.1 Methods

The initial phase of this study involves conducting a comprehensive state-of-the-art review aimed at gaining insights into the characterization, segmentation, and inherent attributes of PCM materials, along with an evaluation of the pros and cons associated with each variant. A analysis process was conduced to determine the optimal selection criteria for identifying the most suitable PCM group to fulfill our specific requirements. A subsequent state-of-the-art review was conducted to explore the various available encapsulation methods for PCM. This review aims to scrutinize the characteristics of each encapsulation technique, with the overarching goal of discerning the most suitable method tailored to our requirements. Following this examination, the study deliberate upon the materials exhibiting the closest alignment with our defined criteria, ultimately culminating in the selection of the most appropriate PCM for our needs.

Subsequent to the comprehensive study and the final selection of both the PCM and encapsulation method, the next step involves the formulation of a calculation model. This model aims to estimate the requisite quantity of PCM necessary to effectively capture

and store solar thermal energy for utilization during non-solar periods within the dryer system. A hourly average for each month of the year solar irradiation data pertinent to the Alcáçovas region in center of Portugal was sourced from the Photovoltaic Geographical Information System (PVGIS) database to inform this estimation process. The geographic region selected for this study was based on the supervisor's expertise.

Succeeding to the preceding steps, the focus will shift towards the verification of the dryer's actual design and the exploration of potential configurations for the PCM STB. This exploration was informed by the estimated volume of PCM derived from the formula developed in the previous step. The aim is to assess and determine the feasibility of integrating PCM STB within the dryer design, considering practical constraints and operational requirements.

Following with the design of a compartment tailored for the PCM STB, utilizing SolidWorks® software and the data already avaliable in the literature, this phase aims to generate a geometric configuration for the STB. Subsequently, a numerical thermal simulation was conducted employing Ansys® software. This simulation seeks to assess the suitability of the geometry, quantity of material, and material properties vis-à-vis our requirements, thereby validating the design's efficacy. The simulation was conducted under both summer and winter conditions, corresponding to the months with the highest and lowest solar irradiance.

For this simulation, it is essential to modify the simulation software's parameters. Specifically, the multiplication factor of the embedded solar calculator must be adjusted to account for the substantial discrepancy between the real data acquired from PVGIS and the calculator's output. Additionally, a mathematical equation representing ambient temperature is required to serve as a temperature boundary condition for the collector's air inlet.

The ensuing step involves an analysis and discussion of the simulation results utilizing Excel® for the data treatment and PowerBI® for the data visualization, both programs from Micrssoft®.

3.2 Definitions

This section contain the definitions necessary to design the desired STB.

3.2.1 Solar Irradiance and correction

The annual solar irradiance and temperature profiles for the Alcaçovas region, located in central Portugal, were obtained from the PVGIS project, the chosen slope of angle was 15 deg which is the standard angle for radiance data collection in PVGIS. The results detailing the global irradiance throughout the year is presented in Figure 3.1.

Month / Hour	Jan	Feb	Mar	Apr	May	Jun	Jul	Aug	Sep	Oct	Nov	Dec
00:00	0,00	0,00	0,00	0,00	0,00	0,00	0,00	0,00	0,00	0,00	0,00	0,00
01:00	0,00	0,00	0,00	0,00	0,00	0,00	0,00	0,00	0,00	0,00	0,00	0,00
02:00	0,00	0,00	0,00	0,00	0,00	0,00	0,00	0,00	0,00	0,00	0,00	0,00
03:00	0,00	0,00	0,00	0,00	0,00	0,00	0,00	0,00	0,00	0,00	0,00	0,00
04:00	0,00	0,00	0,00	0,00	0,00	0,00	0,00	0,00	0,00	0,00	0,00	0,00
05:00	0,00	0,00	0,00	0,00	0,00	0,00	0,00	0,00	0,00	0,00	0,00	0,00
06:00	0,00	0,00	0,00	6,96	51,61	67,65	46,70	12,38	0,00	0,00	0,00	0,00
07:00	0,00	0,00	35,75	139,90	208,40	226,36	200,85	163,73	112,41	43,37	0,00	0,00
08:00	44,06	110,38	211,90	319,88	394,53	408,86	394,48	364,76	309,79	226,77	134,89	54,48
09:00	217,94	293,22	383,02	491,79	559,96	573,75	589,62	570,90	502,69	393,16	292,68	226,92
10:00	360,67	447,05	532,88	625,54	688,16	714,09	763,68	751,64	674,27	536,31	434,00	362,06
11:00	461,70	568,71	648,38	719,18	784,67	831,71	902,47	876,53	781,77	634,00	524,62	464,04
12:00	507,05	606,20	681,79	751,57	827,10	895,07	978,66	946,21	826,11	673,93	555,64	510,73
13:00	505,68	616,00	697,21	745,03	818,66	881,75	981,38	948,51	813,36	648,58	515,17	484,54
14:00	464,82	561,60	637,33	679,84	754,70	822,68	917,68	873,41	728,63	559,50	432,05	419,27
15:00	368,35	465,48	543,74	583,17	657,27	721,82	797,86	749,06	614,33	435,68	336,13	331,06
16:00	241,11	323,25	392,23	448,41	508,28	567,75	628,06	579,67	446,95	285,08	184,43	184,77
17:00	43,61	158,97	223,80	276,64	332,82	383,92	422,40	369,06	243,12	103,08	6,52	0,38
18:00	0,00	0,53	46,43	102,12	151,27	195,79	213,58	155,31	49,63	0,02	0,00	0,00
19:00	0,00	0,00	0,00	0,42	18,83	41,23	41,17	10,84	0,00	0,00	0,00	0,00
20:00	0,00	0,00	0,00	0,00	0,00	0,00	0,00	0,00	0,00	0,00	0,00	0,00
21:00	0,00	0,00	0,00	0,00	0,00	0,00	0,00	0,00	0,00	0,00	0,00	0,00
22:00	0,00	0,00	0,00	0,00	0,00	0,00	0,00	0,00	0,00	0,00	0,00	0,00
23:00	0,00	0,00	0,00	0,00	0,00	0,00	0,00	0,00	0,00	0,00	0,00	0,00

Figure 3.1: Global solar irradiance (W/m^2)

For this study will be used only the direct solar radiation that reaches the surface in the chosen region, as detailed in Subsection 2.2.3.The profile for direct solar radiation data collected from PVGIS is available in Figure 3.2

Month / Hour	Jan	Feb	Mar	Apr	May	Jun	Jul	Aug	Sep	Oct	Nov	Dec
00:00	0,00	0,00	0,00	0,00	0,00	0,00	0,00	0,00	0,00	0,00	0,00	0,00
01:00	0,00	0,00	0,00	0,00	0,00	0,00	0,00	0,00	0,00	0,00	0,00	0,00
02:00	0,00	0,00	0,00	0,00	0,00	0,00	0,00	0,00	0,00	0,00	0,00	0,00
03:00	0,00	0,00	0,00	0,00	0,00	0,00	0,00	0,00	0,00	0,00	0,00	0,00
04:00	0,00	0,00	0,00	0,00	0,00	0,00	0,00	0,00	0,00	0,00	0,00	0,00
05:00	0,00	0,00	0,00	0,00	0,00	0,00	0,00	0,00	0,00	0,00	0,00	0,00
06:00	0,00	0,00	0,00	0,58	12,86	18,19	9,13	0,41	0,00	0,00	0,00	0,00
07:00	0,00	0,00	14,82	68,70	110,02	119,70	106,88	85,77	55,02	20,60	0,00	0,00
08:00	29,49	63,33	117,39	190,09	243,61	253,43	258,33	239,70	192,90	132,19	78,34	35,06
09:00	138,80	184,72	235,59	312,39	364,17	388,07	427,55	417,05	347,54	250,46	183,43	144,32
10:00	237,89	294,35	344,46	405,80	464,86	504,64	586,48	579,16	489,41	361,99	288,59	241,86
11:00	316,45	387,62	427,76	470,75	549,76	599,65	713,51	687,86	573,69	433,45	354,11	322,00
12:00	345,06	407,38	453,58	489,37	571,03	654,11	788,44	751,17	604,00	461,71	374,11	356,75
13:00	349,80	413,18	454,48	469,28	562,67	635,25	790,23	754,27	591,37	437,11	334,30	332,39
14:00	317,15	370,13	402,53	426,15	512,59	587,96	732,19	682,43	522,75	368,07	275,49	279,52
15:00	245,58	299,69	338,19	358,91	437,98	508,17	625,17	573,62	436,14	276,27	210,04	219,40
16:00	157,33	199,95	234,43	271,98	324,86	391,93	478,39	429,76	302,66	171,73	108,08	117,07
17:00	24,71	93,19	122,85	153,51	197,33	248,21	299,50	252,32	148,52	53,87	1,77	0,00
18:00	0,00	0,00	19,26	44,25	73,74	105,43	129,10	83,94	21,36	0,00	0,00	0,00
19:00	0,00	0,00	0,00	0,00	0,01	4,92	7,11	0,06	0,00	0,00	0,00	0,00
20:00	0,00	0,00	0,00	0,00	0,00	0,00	0,00	0,00	0,00	0,00	0,00	0,00
21:00	0,00	0,00	0,00	0,00	0,00	0,00	0,00	0,00	0,00	0,00	0,00	0,00
22:00	0,00	0,00	0,00	0,00	0,00	0,00	0,00	0,00	0,00	0,00	0,00	0,00
23:00	0,00	0,00	0,00	0,00	0,00	0,00	0,00	0,00	0,00	0,00	0,00	0,00

Figure 3.2: Direct solar irradiance (W/m²)

Comparing the data from the simulation software's solar calculator with real data obtained from PVGIS reveals a significant discrepancy between both. To address this, a correction factor must be determined. This requires deriving equations for both the real data and the simulation software's output. These equations were generated using an Excel® tool that fits a polynomial function to the data, similar results can be obtained using the Runge-Kutta method. The resulting for the real data and the solar calculator output are presented in Figure 3.3. As for the equations, Equation 3.1 is refereed to the summer_SC curve, Equation 3.2 is refereed to the summer_real curve, Equation 3.3 is refereed to the winter_SC curve, Equation 3.4 is refereed to the winter_real curve.

Summer Solar Calculator:

$$y = -0,1894x^4 + 10,186x^3 - 211,16x^2 + 2001,6x - 6422,8 \quad R^2 = 0,9834 \tag{3.1}$$

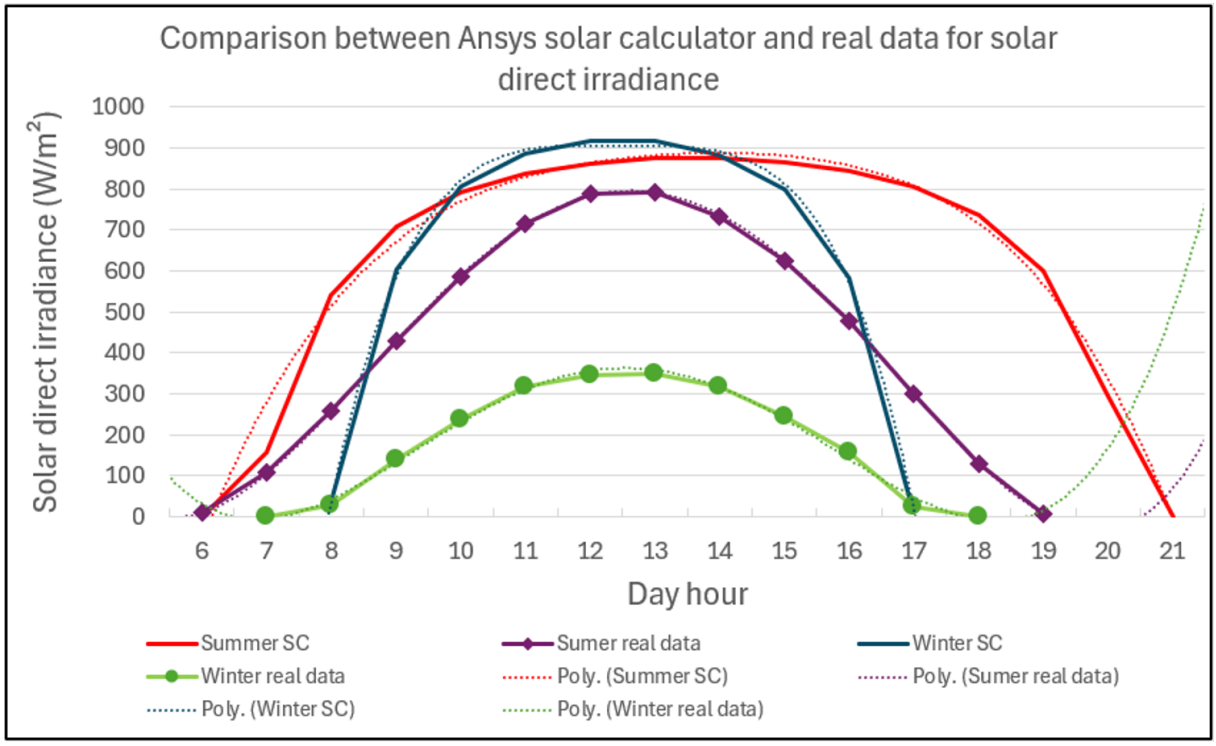

Figure 3.3: Equations for solar irradiance approximation

Summer PVGIS data:

$$y = 0,3128x^4 - 15,857x^3 + 269,57x^2 - 1741x + 3771,1 \quad R^2 = 0,9999 \tag{3.2}$$

Winter Solar Calculator:

$$y = -2,0798x^4 + 103,93x^3 - 1948,9x^2 + 16252x - 49944 \quad R^2 = 0,9988 \tag{3.3}$$

Winter PVGIS data:

$$y = 0,3474x^4 - 17,45x^3 + 305,98x^2 - 2181,7x + 5425,7 \quad R^2 = 0,9933 \tag{3.4}$$

In Figure 3.3, the discrepancy between the Ansys solar calculator (SC) data and the actual data from PVGIS is evident. This comparison highlights the necessity of implementing a correction factor in the simulation software to reconcile the differences.

For each of the polynomial equations (3.2, 3.1, 3.4 and 3.3), the R^2 value is displayed, indicating the fit between the equation and the PVGIS data. As the R^2 value approaches 1, the equation more accurately represents the underlying data [45].

To derive a correction coefficient, it is essential to approximate the area under each curve. This was achieved using the method of definite integration, which, given a known equation and specified integration limits, allows for the calculation of the area beneath the curve. This approach was selected as the area under the curve corresponds to the total solar energy available throughout the day, a crucial factor in TES analysis, where the focus is on total energy availability rather than peak or instantaneous values.

To determine the integration limits, each fourth-order polynomial equation must be solved, yielding four solutions each. The resulting solutions are presented in Table 3.1.

Table 3.1: Solutions for solar irradiation polynomial functions

	Summer SC	Summer PVGIS	Winter SC	Winter PVGIS
x_1	Complex Solution	6,3719	Complex Solution	7,49516
x_2	7,1523	6,7353	8,9556	8,22055
x_3	21,9753	20,1194	18,00658	18,68157
x_4	Complex Solution	21,4665	Complex Solution	19,83397

Based on the solutions of the equations, the lower integration limit, x_2, will be applied across all four equations, representing the time of day when the sun begins to rise. Similarly, the upper integration limit, x_3, will be used for all equations to signify the time when the sun sets. With the integration limits presented in Table 3.1, the integral of each polynomial equations can be solved. The following section presents the simplified calculations along with the corresponding results.

- Summer SC integral results:

$$\int_{7,15234}^{21,97527} -0,1894x^4 + 10,186x^3 - 211,16x^2 + 2001,6x - 6422,8 \; dx = 9890,65295$$

- Summer PVGIS integral results:

$$\int_{6,73533}^{20,11939} 0,3128x^4 - 15,857x^3 + 269,57x^2 - 1741x + 3771,1 \; dx = 5969,92519$$

- Winter SC integral results:

$$\int_{8,95555}^{18,00658} -2,0798x^4 + 103,93x^3 - 1948,9x^2 + 16252x - 49944 \; dx = 6481,84117$$

- Winter PVGIS integral results:

$$\int_{8,22055}^{18,68157} 0,3474x^4 - 17,45x^3 + 305,98x^2 - 2181,7x + 5425,7 \; dx = 2157,23034$$

With the integrals results, it is possible to obtain the ratio between them, the reduction factors for summer and winter are as follows:

- Summer reduction factor: $\frac{5969,92519}{9890,65295} = 0,603593$
- Winter reduction factor: $\frac{2157,23034}{6481,84117} = 0,332811$

Both reduction factors will be used as a solar direct radiation multiplication factor within the simulation definitions.

3.2.2 Ambient temperature

Figure 3.4 illustrates the hourly temperature distribution across the region for each month, as obtained from the PVGIS. This data facilitates the development of a mathematical function to represent the inlet temperature for system simulations. A sinusoidal function was selected for its ease of implementation within the simulation software. The resulting function, along with a comparison to actual temperature data from summer and winter, is shown in Figure 3.5.

The breakdown of the summer sinusoidal equation (Equation 3.5) is as follows:

Hour \ Month	Jan	Feb	Mar	Apr	May	Jun	Jul	Aug	Sep	Oct	Nov	Dec
00:00	8,79	9,01	10,51	12,45	15,19	18,11	20,24	21,01	19,41	16,85	12,19	9,89
01:00	8,48	8,65	10,13	12,04	14,66	17,47	19,49	20,30	18,85	16,47	11,89	9,63
02:00	7,85	8,13	9,72	11,59	14,04	16,87	18,62	19,50	18,26	15,83	11,43	8,86
03:00	7,61	7,86	9,44	11,26	13,66	16,44	18,12	19,00	17,86	15,55	11,23	8,66
04:00	7,41	7,61	9,20	11,00	13,36	16,10	17,72	18,57	17,51	15,31	11,06	8,48
05:00	7,46	7,57	9,13	10,84	13,49	16,32	17,73	18,36	17,35	15,23	11,01	8,55
06:00	7,33	7,38	8,94	10,67	13,46	16,37	17,63	18,09	17,09	15,04	10,88	8,41
07:00	7,23	7,27	8,94	11,23	14,71	17,72	18,74	18,73	17,19	14,91	10,71	8,25
08:00	7,68	7,87	10,11	13,21	16,61	19,40	20,68	21,01	19,16	16,12	11,23	8,78
09:00	8,43	9,35	11,98	14,96	18,49	21,45	22,97	23,43	21,44	18,15	12,69	9,64
10:00	10,26	11,29	13,71	16,55	20,23	23,38	25,27	25,87	23,64	20,04	14,42	11,43
11:00	11,31	12,29	14,37	16,98	20,69	24,01	26,23	27,02	24,87	21,11	15,36	12,37
12:00	12,55	13,53	15,55	17,98	21,82	25,32	27,95	28,79	26,32	22,29	16,43	13,60
13:00	13,41	14,38	16,37	18,67	22,59	26,24	29,23	30,07	27,31	23,07	17,10	14,42
14:00	13,93	14,85	17,07	19,20	23,24	27,06	30,67	31,29	28,06	23,58	17,49	15,08
15:00	14,05	14,99	17,18	19,20	23,30	27,20	30,98	31,60	28,18	23,60	17,41	15,12
16:00	13,80	14,81	16,99	18,94	23,01	26,95	30,77	31,39	27,80	23,20	16,97	14,75
17:00	12,60	13,86	16,39	18,59	22,51	26,28	30,20	30,54	26,60	21,74	15,53	13,23
18:00	11,41	12,70	15,37	17,67	21,49	25,16	28,91	29,16	25,21	20,35	14,38	12,08
19:00	10,58	11,54	13,96	16,29	20,03	23,56	27,02	27,18	23,52	19,20	13,63	11,34
20:00	9,89	10,36	12,44	14,52	18,07	21,67	24,83	25,08	21,84	18,32	12,99	10,73
21:00	9,34	9,67	11,60	13,59	16,86	20,24	23,17	23,58	20,77	17,57	12,46	10,26
22:00	8,89	9,11	10,92	12,83	15,93	19,13	21,85	22,36	19,90	16,94	12,03	9,86
23:00	9,09	9,43	11,04	12,98	16,00	18,89	21,16	21,89	19,93	17,20	12,34	10,18

Figure 3.4: Temperature profile (K)

$$6,675[K] \cdot \sin\left(\frac{t[s] - 34200[s]}{86400[s]/\pi}\right) + 297,455[K] \tag{3.5}$$

Where:

- $6,675[K]$ represents the amplitude of the sinusoidal function, which corresponds to the difference between the maximum and minimum daily temperatures.
- $t[s]$ is the transient time step in seconds during the simulation, varying according to the simulation step.
- $-34200[s]$ accounts for the phase shift of the function. Since the simulation starts at midnight, the zero point of the sinusoidal function must match the ambient temperature at midnight and be in the descending phase, as the minimum temperature

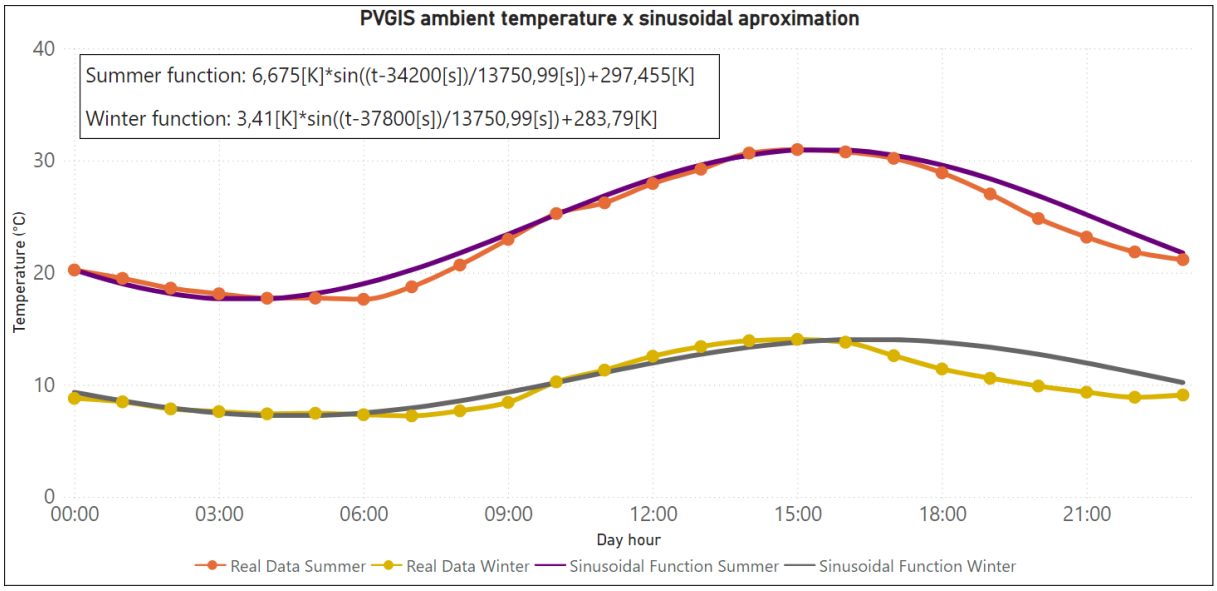

Figure 3.5: Temperature function approximation (K)

typically occurs between 06:00 and 07:00. To match it, a 9:30 hours correction need to me made, witch results in the -34200 seconds. For each Geo-position and each season this parameter must be adjusted.

- $86400[s]/\pi$ corresponds to the total wave period, where $86400[s]$ represents the total number of seconds in a day. The division by π ensures the correct scaling for the sine function.

- $297,455[K]$ shifts the function upwards to align it with the average daily temperature.

The results of the summer and winter sinusoidal temperature functions are displayed in Figure 3.5. Each of these functions will be applied as a boundary condition for the inlet ambient temperature in the simulation setup.

An alternative method explored was the sixth-order Runge-Kutta approach to approximate ambient temperature using a sixth-order polynomial. Although this method provided a more accurate fit compared to the sinusoidal model, its implementation within the simulation software was not feasible. As a result, the sinusoidal model was chosen for the simulations.

3.2.3 PCM Selection Criteria

The criteria for selecting PCMs in this study are based on the considerations outlined in 2.2.2.

For the purposes of this study, the following criteria were prioritized based on their importance:

1. Melting Temperature within the desired operating range: the operational temperature of the dryer should be close to 40°C.

2. Cost-effectiveness: The PCM should be priced at or below $1 per kilogram to ensure an affordable solution.

3. High Latent Heat of Fusion per Unit Volume: A PCM with a latent heat of fusion above 200 kJ/kg is preferred to minimize the required quantity of material and reduce costs.

4. Durability Against Solidification/Melting Cycles: The selected PCM should exhibit no degradation even after undergoing numerous solidification/melting cycles, ensuring longevity and reliability of the equipment.

The melting temperature serves as the primary selection parameter due to its direct relevance to equipment operation temperatures. Cost-effectiveness follows as a key objective to achieve an affordable solution. Additionally, a high latent heat of fusion is desirable to maximize thermal energy storage efficiency and reduce material requirements. Lastly, the PCM must maintain its performance integrity over an extended lifespan, capable of enduring frequent solidification/melting cycles without degradation.

Based on these parameters, a wide variety of PCM categories can be excluded. Figure 3.6 illustrates the classification of PCM groups according to their melting enthalpy and fusion temperature according to [46].

Based on the first selection criterion, groups 1 (Eutectic water-salt solutions), 2 (Gas hydrates), 6 (Water), 8 (Nitrates), 10 (Hydroxides), 11 (Chlorides), 12 (Carbonates), and

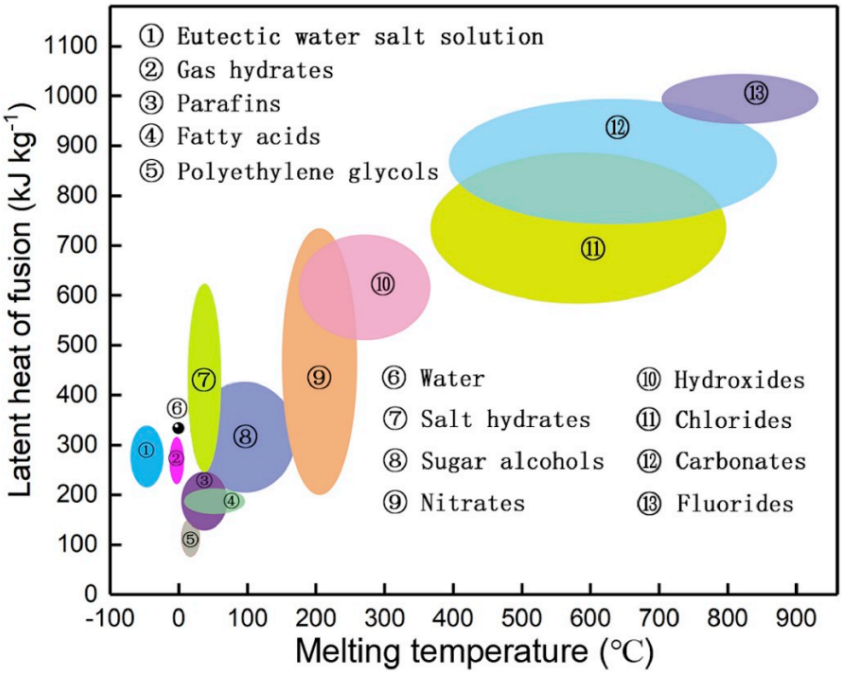

Figure 3.6: PCM Grups segmentation by [46]

13 (Fluorides) are excluded due to, must of their melting temperatures not being close to 40°C. Moving to the third selection criterion, groups 3, 4, and 5 (Paraffins, fatty acids, and polyethylene glycols) are excluded as their melting enthalpy is below $200kJ/kg$. The final group remaining is the salt hydrates, which will be the focus for material selection.

3.2.4 Material quantity and thermal storage price

The calculation of the requisite material quantity for storing available energy entails employing Equation 3.6, derived from Equation 2.1 and Equation 2.2. The energy necessitating storage comprises above zero values indicative of thermal energy availability, as observed notably in July, boasting a positive thermal energy surplus of $28362,92kJ/m^2$ over a 12-hour duration, as depicted in Figure 3.1. Equation 3.6 serves the purpose of delineating the requisite material quantity in kilograms per square meter of solar thermal collection area.

$$z \cdot \rho = \frac{(3600/1000) \cdot \int_a^b I_{hi}\, dx}{(C_{ps} \cdot \Delta K_s + C_{pl} \cdot \Delta K_l) + \Delta H} \tag{3.6}$$

Where:

- z (m) is the height of the TES.
- ρ (kg/m^3) is the PCM density.
- $\int_a^b I_{hi}\, dx$ (W/m^2) is the integral of the month hourly radiation polynomial equation, it is possible to see the equation that follows the chosen geographic region in Figure 3.3. The limits of the integral is defined as the solutions for the polynomial equation, as shown in Table 3.1. The lower limit represents the hour at which solar radiation begins (sunrise), while the upper limit indicates the hour at which solar radiation ceases (sunset).
- 3600/1000 $(s/1)$ is the seconds in one hour with the objective of transforming W/m^2 in kJ/m^2.
- C_{ps} (kJ/kgK) is the solid specific heat of the PCM.
- ΔK_s (K) is the temperature variation in solid state of the PCM.
- C_{pl} (kJ/kgK) is the liquid specific heat of the PCM
- ΔK_l (K) is the temperature variation in liquid state of the PCM.
- ΔH (kJ/kg) is the enthalpy of fusion of the PCM.

The result of this equation represents the amount of material required to store the calculated thermal energy per square meter (m^2). Since solar irradiation is commonly measured in m^2, it is appropriate to use a related unit for the material required to store the energy. This allows for a direct correlation between the collector's area and the volume of material necessary for the TES system.

Equation 3.6 represents a general formulation for global applications. However, for this study, discrete PVGIS data is employed. To accommodate the use of discrete data rather than a continuous equation, the integral in Equation 3.6 must be converted into a summation, expressed as $\sum_{i=0}^{23} I_{hi}$, resulting in Equation 3.7. In this summation, the index i denotes the specific hour of the day, while I_{hi} represents the solar energy available during the respective hour.

$$z \cdot \rho = \frac{(3600/1000) \cdot \sum_{i=0}^{23} I_{hi}}{(C_{ps} \cdot \Delta K_s + C_{pl} \cdot \Delta K_l) + \Delta H} \tag{3.7}$$

3.2.5 Material Selection

Material selection was gathered by a comprehensive investigation, as detailed in the study by [22], which provides a thorough analysis encompassing a wide array of PCM types spanning various classifications, including organic and inorganic variants. Drawing upon this research, parameters for material selection elucidated in 3.2.3, facilitated the segregation of desirable salt hydrates. The outcome of this segregation process is presented in Table 3.2.

Table 3.2: Selected salt hydrates

Salt Hydrate	Formula	CAS Number	Abreviation
Sodium Sulfate Decahydrate	Na2 SO4 · 10H2O	7757-82-6	SSD
Sodium Carbonate Decahydrate	Na2 SO3 · 10H2O	497-19-8	SCD
Sodium Hydrogen Phosphate Dodecahydrate	Na2 HPO4 · 12H2O	7558-79-4	SHPD
Iron (III) Chloride Hexahydrate	FeCl3 · 6H2O	7705-08-0	ICH
Potassium Fluoride Dihydrate	KF · 2H2O	7789-23-3	PFD
Magnesium Sulfate Heptahydrate	MgSO4 · 7H2O	7487-88-9	MSH
Sodium Thiosulfate Pentahydrate	Na2S2O3 · 5H2O	7772-98-7	STP
Sodium Acetate Trihydrate	CH3COONa · 3H2O	127-09-3	SAT
Sodium Hydroxide Monohydrate	NaOH · H2O	1310-73-2	SHM
Iron (II) Sulfate Heptahydrate	FeSO4 · 7H2O	7720-78-7	ISH

Therefore, utilizing the Equation 3.7, was possible to do a comprehensible comparison of the total material price for each material. The results are presented in Table 3.3.

Table 3.3: Material evaluation

Salt	Melting temp (°C)	Melting entalpy (kJ/kg)	Density (kg/m^3)	Material price (€/kg)	Quantity (kg/m^2)	Parametric material price (€/m^2)
SSD	31,70	245,10	1477	0,06	90,26	5,20
SCD	33,45	215,40	1447	0,21	99,98	21,12
SHPD	36,85	232,85	1521	0,68	94,72	64,56
ICH	36,55	206,10	1600	0,43	103,96	44,91
PFD	41,50	214,00	1658	0,90	101,93	91,98
MSH	48,60	201,50	1680	0,26	108,17	28,56
STP	48,00	204,50	1708	0,21	106,83	22,56
SAT	57,95	234,50	1450	0,45	97,63	43,58
SHM	61,76	272,20	1710	0,32	86,92	27,54
ISH	64,00	200,00	1890	0,15	112,11	16,68

Based on Table 3.3 and the selection criteria outlined in the 3.2.3 subsection, the materials chosen for simulation under summer and winter conditions are SSD, STP and ISH.

These materials were selected due to their low cost per square meter €/m^2, possible to observe in the last column from Table 3.3, and their suitable melting temperature ranges (31°C, 48°C, and 64°C). This allows for an evaluation of the varying performance of each material under both summer and winter conditions.

Table 3.3 presents the properties of each selected material. These properties will be input into the simulation software to conduct the simulations.

The chosen encapsulation method is macro-encapsulation, as it is better suited for applications with larger energy variations, whereas micro-encapsulation is typically used for scenarios with smaller energy fluctuations. Macro-encapsulation allows for the utilization of a larger volume of PCM, making it more appropriate for this study. This method was also employed in the experiment conducted by [47], and the encapsulation geometry in this work will follow the same approach used in that experiment.

Other parameters that will be utilized, as not all materials have their thermal properties comprehensively documented in the literature, will remain constant across all three

PCM materials. These parameters are the sensible heat of $1500\,J/(kg \cdot K)$ and thermal conductivity of $0,7\,W/(m \cdot K)$. This means that for all materials that does not contain extensive literature data related to their thermal proprieties, those values ware utilizes as a way to approximate to its real word utilization.

Due to the reasons mentioned previously, particularly the limited availability of thermal property data for the materials, certain properties were kept constant across all materials for the quantity calculations. It is assumed that all materials are subject to the same ambient conditions. The following properties were standardized for the calculations are solid sensible heat of $1000\,J/(kg \cdot K)$, liquid sensible heat of $1500\,J/(kg \cdot K)$, lower temperature of 20°C and upper temperature of 70°C.

The values for the solid and liquid sensible heat were estimated based on data by [22], while the temperature range was determined by considering the radiation energy provided by PVGIS (as shown in Table 3.1) and the latent heat of the materials.

3.3 3D Modeling

The 3D geometry definitions for the solar thermal collector were established from [47], . Key parameters were identified, such as the length of the collector, the air intake geometry, were identified. For air inlet velocity, the parameter was collected from [6]. These parameters will serve as boundary conditions for the simulation. Figure 3.7 provides a representation of the solar collector used for paraffin thermal storage, as described in [47].

In addition, glass parameters, such as thickness and absorptivity, were obtained from [48].

By utilizing data such as the plane slope from PVGIS, the amount of material required to store solar irradiation, and the collector area obtained from previous analyses as well as studies by [47] and [49] for the air canal design, a design was developes for the solar collector integrated with the TES.

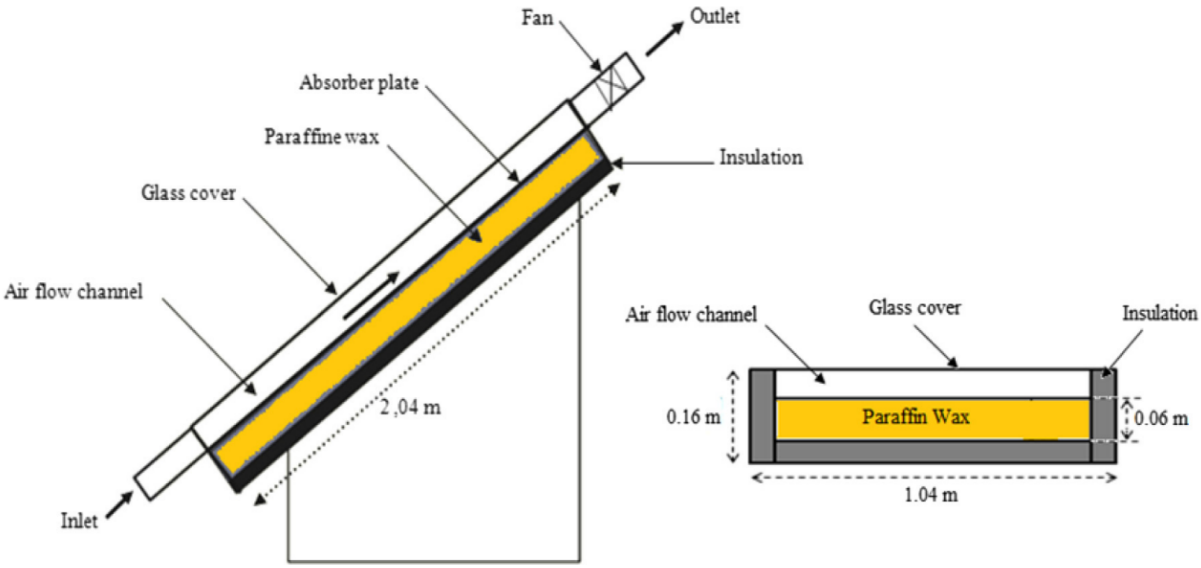

Figure 3.7: Solar collector representation from [47].

3.3.1 Technical drawing

Continuing with the 3D modeling process, Figures 3.8 and 3.9 illustrate the results of the modeling, along with the designation of each component of the solar collector. Figure 3.8 presents the dimensions of the solar collector to be simulated, while Figure 3.9 displays the nomenclature adopted to facilitate the discussions and analysis in subsequent sections of this study.

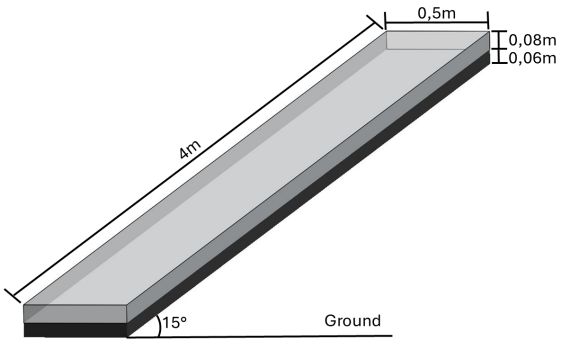

Figure 3.8: Solar collector drawing

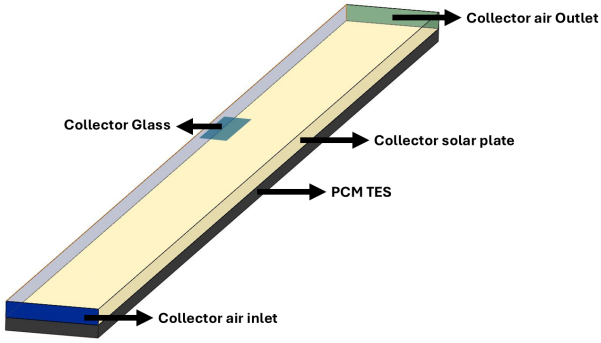

Figure 3.9: Solar collector nominations

3.4 Numerical model

This section presents and elaborates on the definitions and results obtained from the numerical simulations, beginning with mesh definitions and sensitivity analysis to enhance numerical calculation precision. It then continues with the setup in Fluent, including boundary conditions, graph and contour definitions, and concludes with the final simulation results.

3.4.1 Mesh definitions and sensitivity analysis

To ensure accurate simulations, it is essential to use a mesh that can reliably replicate real-world conditions. A mesh sensitivity analysis was conducted, testing six different mesh configurations to identify the one that offered the best balance between simulation time and precision.

Table 3.4: Mesh sensitivity analysis results

Mesh configuration	Default	Default	Default	Default	Default	Inflated mesh[1]	Inflated mesh[2]
Element Size (mm)	50	25	10	5	2,5	10	10
Nodes	4455	27048	327216	2427030	18664458	1753445	342036
Elements	3200	22400	300000	2320000	18240000	1027329	1155782
Element quality	0,936	0,940	0,966	0,966	0,966	1,000	1,000
Aspect ratio	1,697	1,294	1,188	1,103	1,061	52,255	78,954
Skewness	0,167	0,167	0,167	0,167	0,167	0,800	0,812
Ortogonality	0,966	0,966	0,966	0,966	0,966	0,999	0,996
Simulation Time (min)	3	7	14	183	*	70	68
Delta heat flux (W/m^2)	400	260	120	60	*	7	4

[1] Hexagonal pattern, inflation of first layer thickness of 0.5mm, 4 layers, 1,6 growth ratio
[2] Hexagonal pattern, inflation of smooth transition with 6 layers and 1,3 growth ratio
* Simulation did not complete

Table 3.4 presents the configurations used for each mesh tested, along with the corresponding simulation duration and the Delta heat flux, witch is a report data from Ansys, it calculate the energy transfer related to the element area, a more refined mesh results in a lower delta heat flux as the delta is related to the difference between the maximin and

minimum values from this report during the simulation. A lower Delta heat flux indicates higher simulation accuracy.

In Figure 3.10, the results of the mesh sensitivity analysis are presented, along with the geometry of the final mesh configuration. This mesh was selected based on its optimal balance between accuracy and simulation efficiency as previous mentioned.

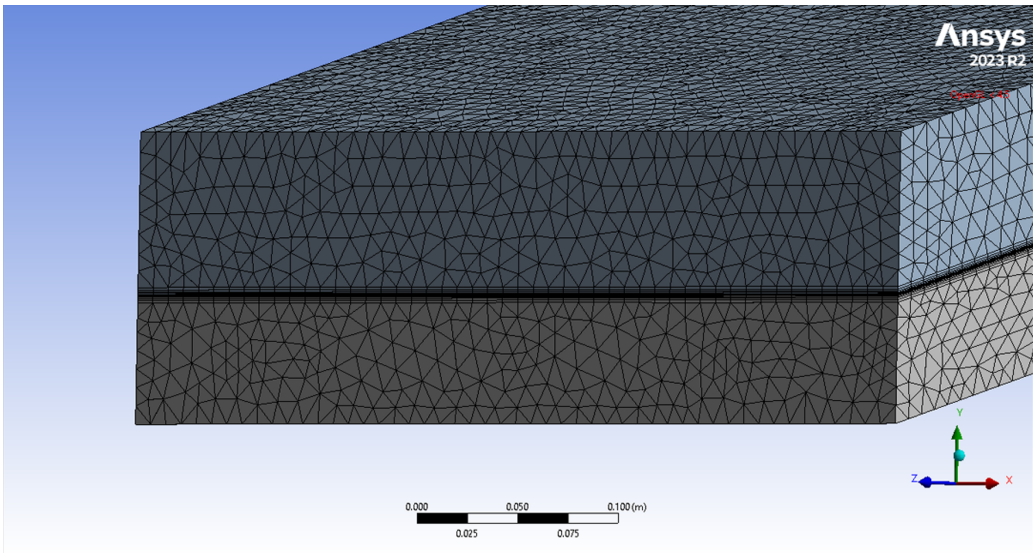

Figure 3.10: Final mesh definitions

3.4.2 Numerical solution definition

The numerical model was developed in ANSYS Fluent to simulate the thermal behavior and performance of PCM. Key parameters and fluid properties were defined to ensure accurate simulation of both the PCM and airflow. The model configuration considers transient conditions. Specific settings include boundary condition assignments aligned with ambient and solar energy data as mentioned before.

Material Properties and Simulation Setup

For air, selected PCMs, aluminum and glass properties were set as despised in Table 3.5. Other proprieties from the categorized PCMs are shown in Section 3.2.5.

For the simulation routine, and the convergence parameters ware decided as follows:

Table 3.5: Material proprieties for system simulation

	Air	PCMs	Aluminium	Glass
Density (kg/m^3)	1,23	1477-1890	2719	1600
Specific Heat (J/(kg K))	1006	1500	871	850
Thermal conductivity (W/(m K))	0,02	0,7	202,4	1,3
Viscosity (kg/(m s))	$1,79 \cdot 10^{-5}$	-	-	-
Latent Heat (kJ/kg)	-	200-245,1	-	-
Melting temperature (K)	-	304,85-339,15	-	-

- The initial conditions for each material in the first simulations were set to match the ambient temperature. Consequently, all components of the system were initialized at the same temperature as defined by the sinusoidal equation for ambient temperature at a specified time of day.

- For subsequent days, if the system temperature at the end of the simulation day fell outside the phase change range, the average temperature of the PCM at the conclusion of the previous simulation day was used as the input parameter for the following day's simulation. In contrast, if the PCM temperature was within the phase change range, a linear approximation was applied to ensure that the amount of energy stored in the PCM remained consistent between simulations. This approach was necessary because ANSYS employs a delta temperature to define the phase change threshold. In this study, a delta phase change temperature of 2 degrees was utilized, meaning that if the PCM, for example the SSD phase change at 31,70°C, in the simulation it will start phase change at 30,70°C and reach full liquid state at 32,70°C, the values in between 30,70°C and 32,70°C is considered phase change temperature range.

- The convergence criteria were defined such that a variation of less than 1 degree in the PCM temperature, when not undergoing a phase change, or a change of less than 1% in the degree of liquefaction/solidification between the start and end of the simulation was considered indicative of convergence, thus concluding the simulation.

The comparison parameter consists of a control simulation that mirrors all parameters and configurations utilized in the PCM simulations. However, this control simulation will be absent of any PCM, allowing for a direct comparison of the simulation's effectiveness and the utility of the TES system.

Computational Parameters

The computational parameters of the simulation were established to ensure precision while optimizing efficiency. A time-stepping approach was used with a total of 144 time steps per cycle, each with a duration of 600 s. This configuration enables accurate tracking of transient thermal behaviors throughout the simulation period (1 complete day per simulation run-trough).

The maximum number of iterations per time step was set to 5. This parameter allows for early convergence when the solution reaches stability before completing all iterations, effectively advancing the simulation to the next time step without unnecessary calculations.

The computer utilized was a virtual machine, provided by Instituto Politécnico de Bragança (IPB), with 32GB of ram and 8 logical processors of an AMD Threadripper 3970x at a base clock speed of 3,7 Ghz. In the Fluent start, 7 logical processors ware utilized for parallel simulation computation to decrease computational time.

3.4.3 Boundary conditions

This part outlines the boundary conditions for the thermal model, including configurations for the air inlet, interior spaces, outlet, air wall, connection plate, PCM walls, and the glass wall.

Air Inlet: The air inlet was configured to account for temperature variations during both summer and winter according to the equations developed in the Ambient Temperature subsection, with no solar participation included in this model. A velocity inlet of 0.5 m/s was established to ensure a consistent flow of air into the system, facilitating

accurate simulations of thermal dynamics based on the mass output of [17].

Interiors: No specific configuration was necessary for the interior boundaries, allowing for a simplified approach to the modeling of internal thermal interactions.

Outlet: The outlet boundary was defined as an outflow condition, with no solar participation considered. This setup allows for the free egress of air from the system.

Collector walls that make contact with the air: those walls was treated as an opaque boundary with a solar absorptance of 0, preventing any solar energy absorption in those walls. The thermal configuration for this wall was established by system coupling, ensuring that the heat transfer characteristics are accurately represented within the overall thermal model. Note: connection plate is not included in this situation.

Connection Plate and Connection Plate Shadow: The connection plate was modeled with a thermal coupling condition, consisting of a single layer of 1 mm aluminum. This opaque body was configured with active solar ray tracing, achieving a direct visible absorptance of 0,99 and a direct infrared absorptance of 0,99.

PCM Walls: PCM walls were defined to not participate in solar radiation, adhering to a thermal system coupling condition. Allowing for accurate modeling of the thermal behavior of the PCM without the influence of external solar radiation, ensuring that the heat transfer dynamics within the system are correctly represented.

Glass wall: was set with a thermal coupling condition and a thickness of 3 mm to simulate its interaction with solar radiation. This semitransparent wall was defined with absorptivity values of 0,04 for direct visible, direct infrared (IR), and diffuse hemispherical radiation, reflecting minimal absorption across these wavelengths. Corresponding transmissivity factors were set to 0,96, allowing for high transparency and aligning with documented glass properties [48].

Solution method: was selected the SIMPLE method which was the standard selection in the software but it too is the best method when the time step for the simulation is considered large, and this is the case for the simulations from this work.

3.4.4 Report Definitions

The following key parameters were defined for the simulation reports:

- **PCM Liquid Fraction**: This parameter quantifies the proportion of the PCM that has transitioned from solid to liquid during the simulation.
- **PCM Average Temperature**: This metric represents the mean temperature of the PCM during the simulation. It is important for assessing the thermal performance PCM in absorbing and releasing thermal energy.
- **Inlet Average Temperature**: The average temperature of the air entering the system.
- **Outlet Average Temperature**: This value indicates the mean temperature of the air exiting the system. It serves as an essential performance indicator, reflecting the effectiveness of the heat exchange processes within the system and the role of the PCM in temperature regulation.

Initialization parameters for the simulation were defined at the commencement of each run. These parameters included the starting temperature of the system, ensuring that the simulations began under consistent conditions for accurate comparisons.

For the visualization of simulation results, contours were selected to represent the middle plane view for both the temperature distribution and the PCM liquefaction rate. Additionally, an isometric view of the system temperature was generated, which includes representations of the inlet and outlet temperatures.

Chapter 4

Results and Discussions

This section presents the results obtained from the simulation, including the temperature evolution throughout the process, the PCM liquefaction factor, which represents the proportion of phase change occurring in the PCM during the simulation, and the output energy generated over the course of the simulated day.

For the presentation of the results, the mid-plane was selected due to its suitability for visualizing both the air and PCM temperatures within the system. Figure 4.1 illustrates the location of this plane in the y-z axis, providing a clear representation of the system's thermal distribution.

Figure 4.3 illustrates the system's temperature distribution, revealing a homogeneous temperature profile. Given this uniformity, it is feasible to focus solely on the temperature at the mid-plane, as it accurately reflects the thermal state of the entire system.

Related to the results collection, as mentioned in Subsection 3.4.2, after the system stabilization. Figure 4.2 show the stabilization process for all PCM stabilization.

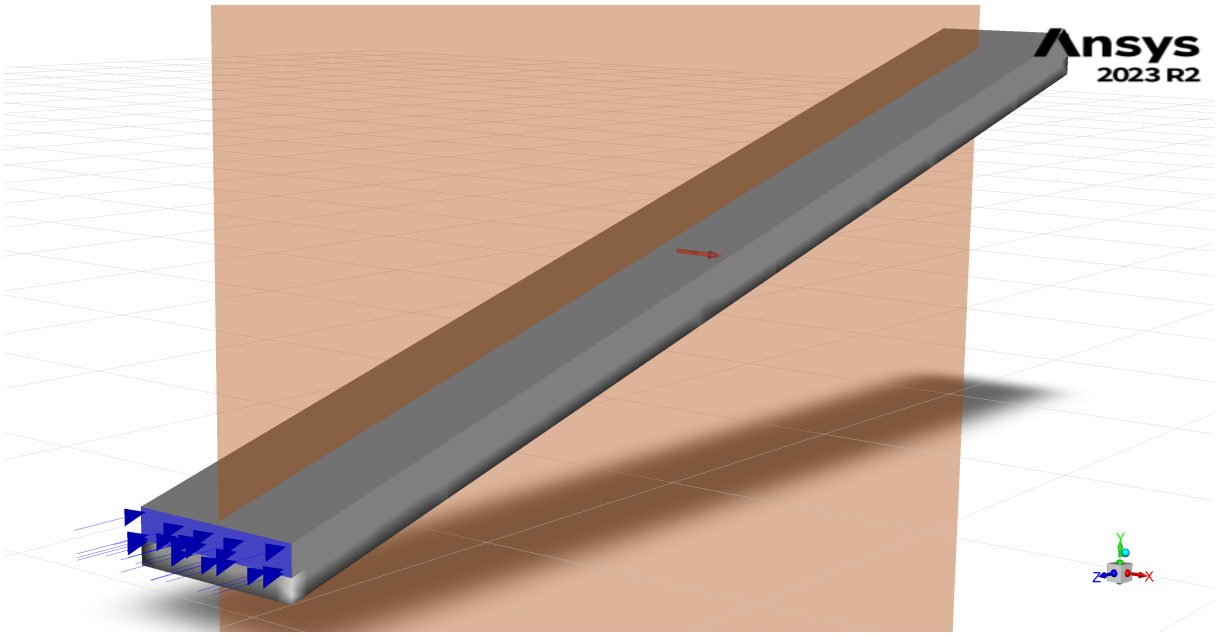

Figure 4.1: Mid plane visualization

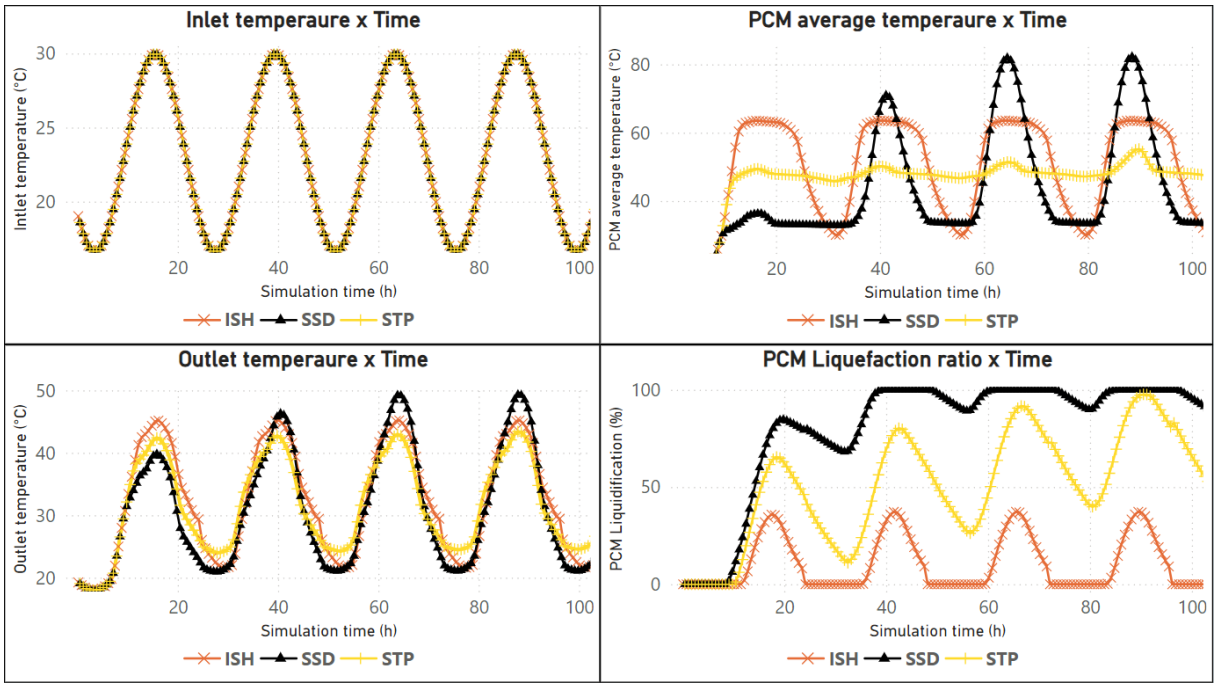

Figure 4.2: Simulation stabilization

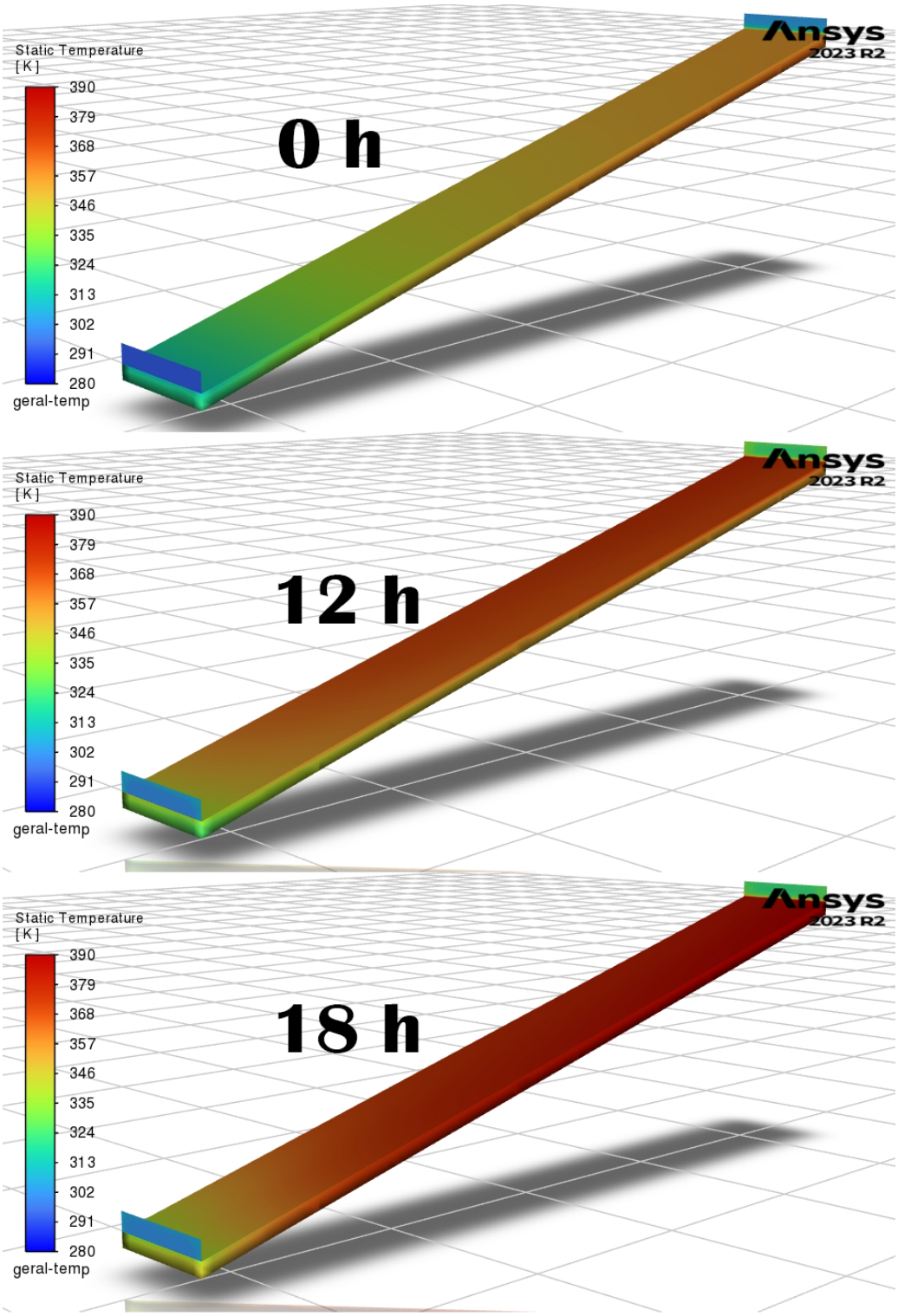

Figure 4.3: System temperature

4.1 Temperature evaluation

This section details the temperature evolution and analysis for both summer and winter simulations.

4.1.1 Summer

In Figure 4.6, the temperature evolution throughout the simulation hours is depicted. On the figure, the mid-plane temperature is presented. In the control case, only the air temperature is visible, as no PCM is present. The figure illustrates temperature progression at key points during the day: the beginning at 0h, midday at 12h, and 18h, when low to no solar radiation reaches the collector.

Similar to Figure 4.6, Figures 4.5 and 4.4 present the temperature contours at the same key times (0h, 12h, and 18h) for the other three selected PCM. These figures provide a comparative view of the temperature evolution for each PCM.

The comparison of the temperature evolution among the three selected PCMs reveals that the simulation with the greatest temperature delta between midnight and the peak daytime temperature was the control case, as shown in Figure 4.6. This highlights the effect of the absence of PCM on temperature regulation, with the control case experiencing more pronounced fluctuations. The part of the figure that shows the 12h mark shows that the right top part of the collector is at a greater temperature, with relates with the correct system operation.

Continuing with the analysis of temperature evolution, Figures 4.6, 4.5 and 4.4 display the temperature contours at specific time steps within the transient simulation. To provide a more comprehensive view, the subsequent figures will present the full temperature evolution throughout the entire simulation period.

Figure 4.7a illustrates the inlet temperature variation over time, following the sinusoidal pattern described in Subsection 3.2.2. This figure displays the output data from Ansys, confirming that the implementation of the temperature function was successful and that the results align with the expected behavior for the inlet temperature.

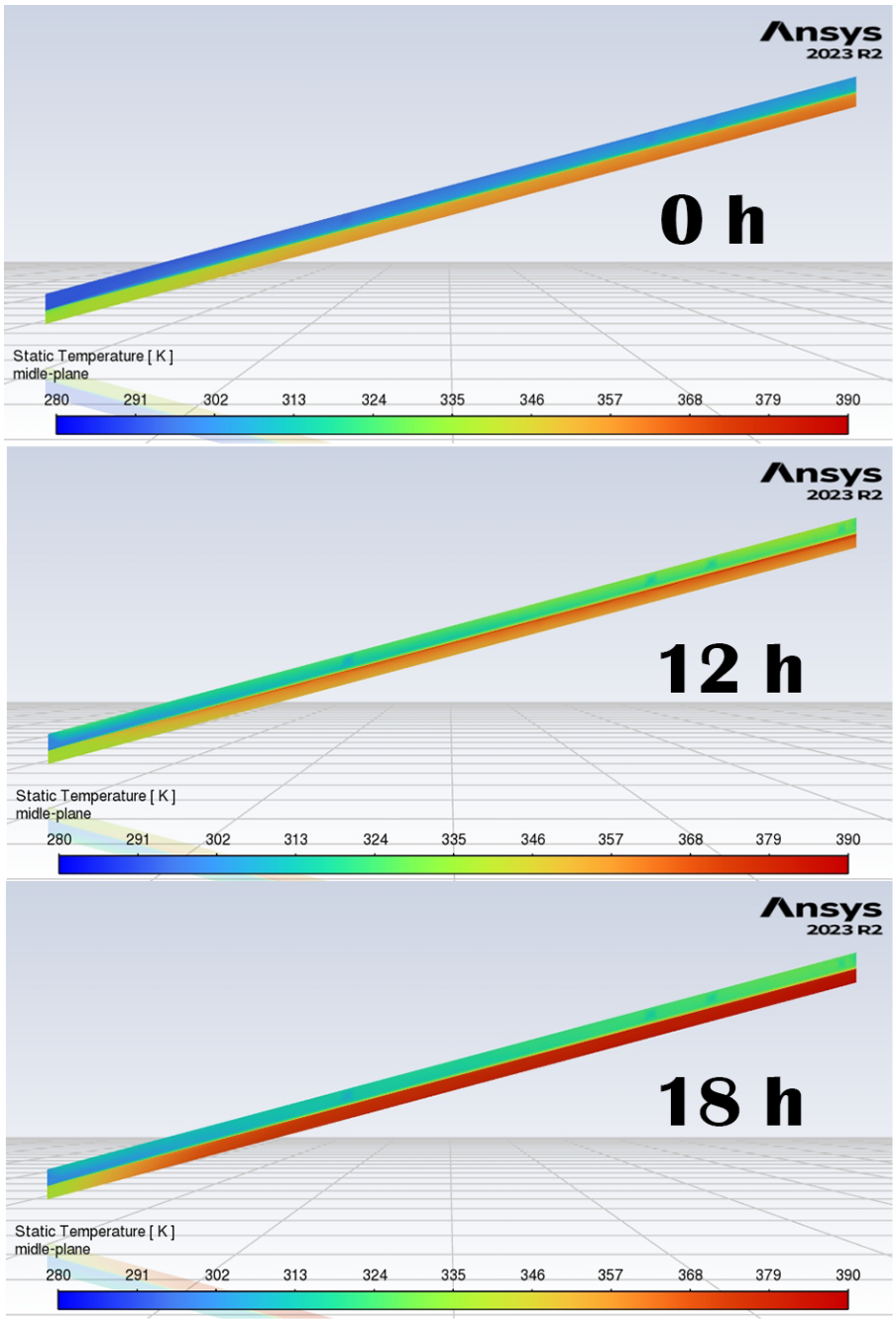

Figure 4.4: Summer ISH and STP temperature contours

Continuing with the analysis of the airflow through the solar collector, Figure 4.7b shows the temperature evolution at the collector's outlet. The figure highlights the temperature differences between the systems utilizing PCM and the control system without any TES. A notable observation is the more pronounced temperature fluctuations in the

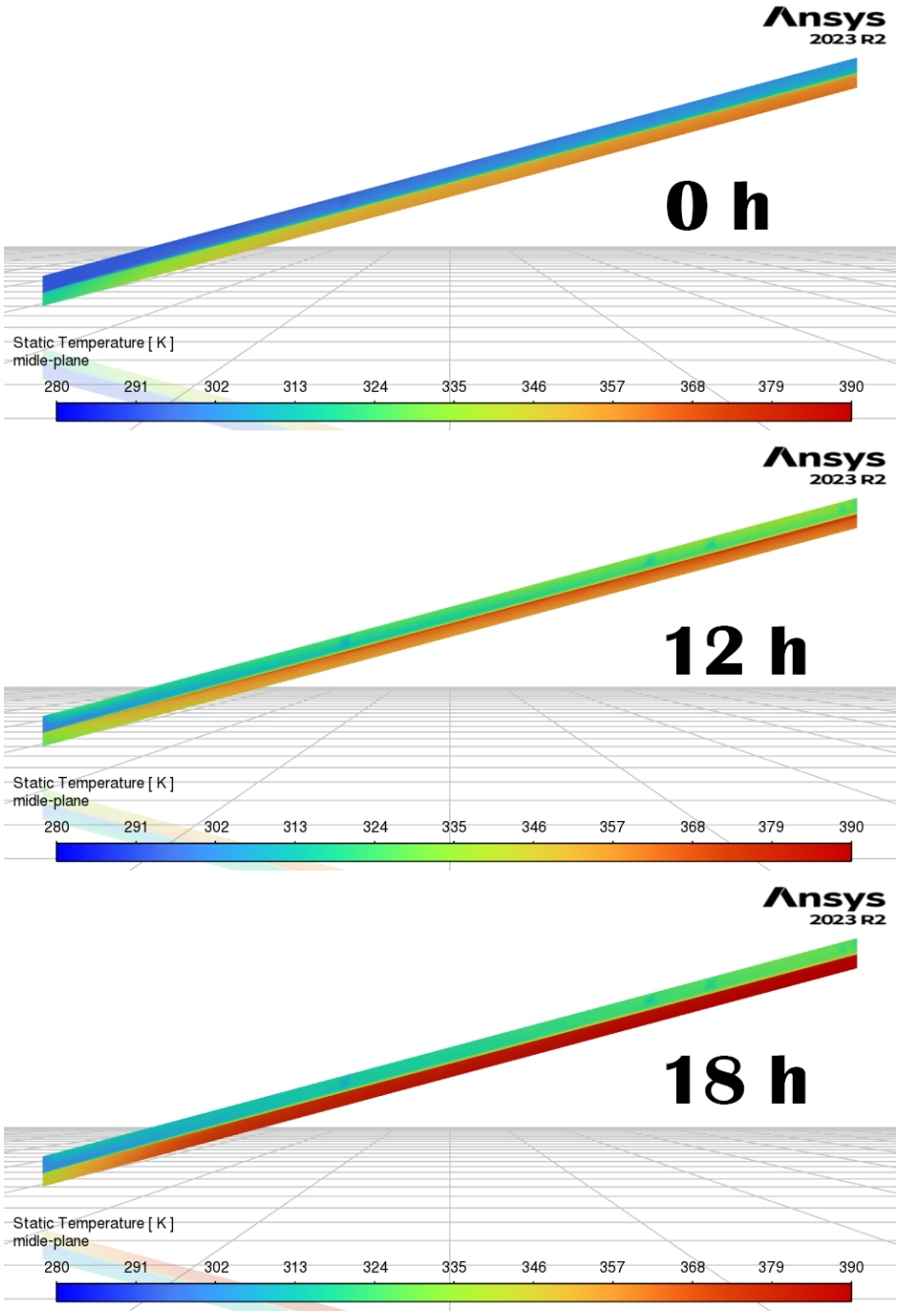

Figure 4.5: Summer SSD temperature contours

control system compared to the systems with PCM, with all three PCMs maintaining a more stable outlet temperature. Additionally, the PCM that exhibited the most consistent temperature regulation was ISH, which is attributed to its phase change temperature.

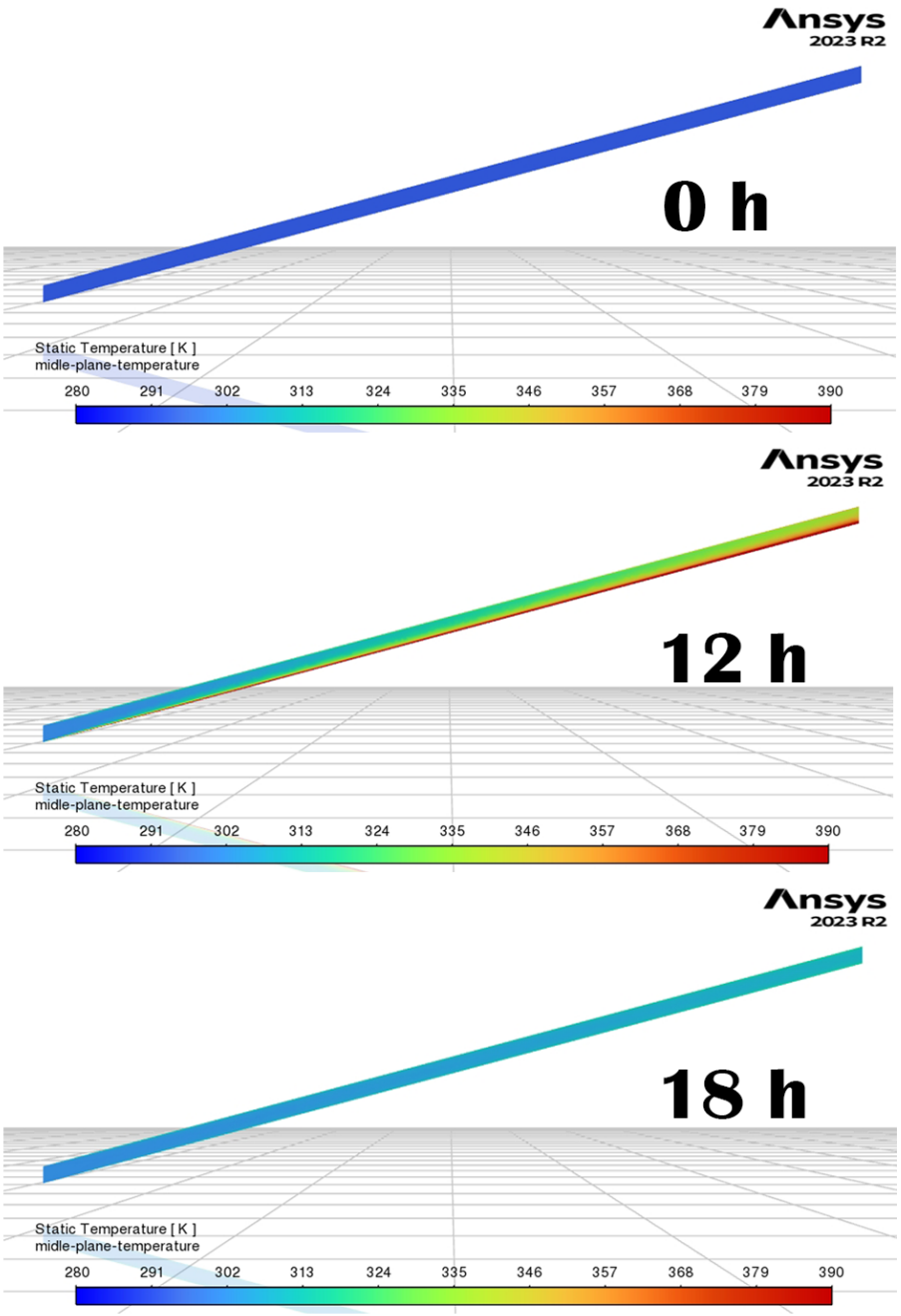

Figure 4.6: Summer Control temperature contours.

This stability is clearly visible in Figures 4.7b and 4.7c, where the temperature amplitude of the ISH system is smaller compared to SSD and STP. A lower amplitude between the highest and lowest temperatures indicates a more consistent outlet temperature. Such consistency in the outlet temperature simplifies the planning and development of systems

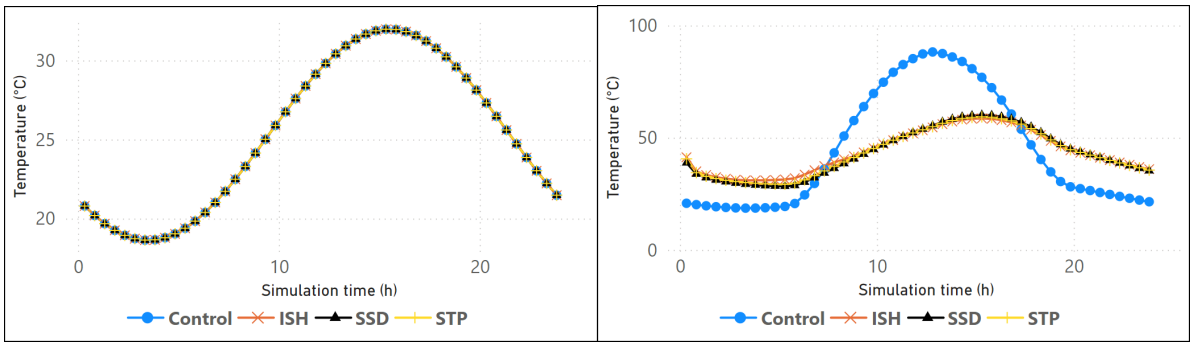

(a) Summer inlet temperature (b) Summer outlet temperature

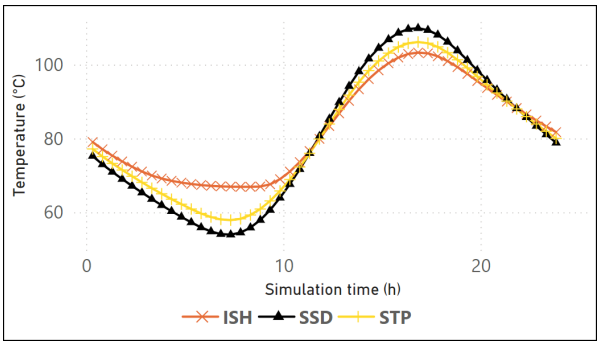

(c) Summer average PCM temp

Figure 4.7: Summer temperature profiles

that incorporate STB, enabling more predictable and efficient thermal management.

Continuing with the analysis of temperature evolution across each simulation, Figure 4.8 depict the progression of inlet, outlet, and PCM temperatures, alongside the liquefaction fraction of the PCM. The temperature variation is presented in the lower graph of each figure, while the upper graph illustrates the liquefaction rate. The specific PCM material under evaluation is indicated in the title of the upper graph for each figure.

Analyzing Figure 4.8, it is evident that Figure 4.8a shows the largest temperature differential, which is attributed to the absence of any TES. Another key observation is that the inlet and outlet temperatures in the control simulation remain constant during non-solar hours, accurately reflecting real-world conditions and further validating the precision of the simulation setup and boundary conditions. Among the simulated PCMs, only ISH (Figure 4.8d) exhibits distinct behavior, as it is the only material undergoing a phase change. During the phase change process, the outlet temperature remains relatively

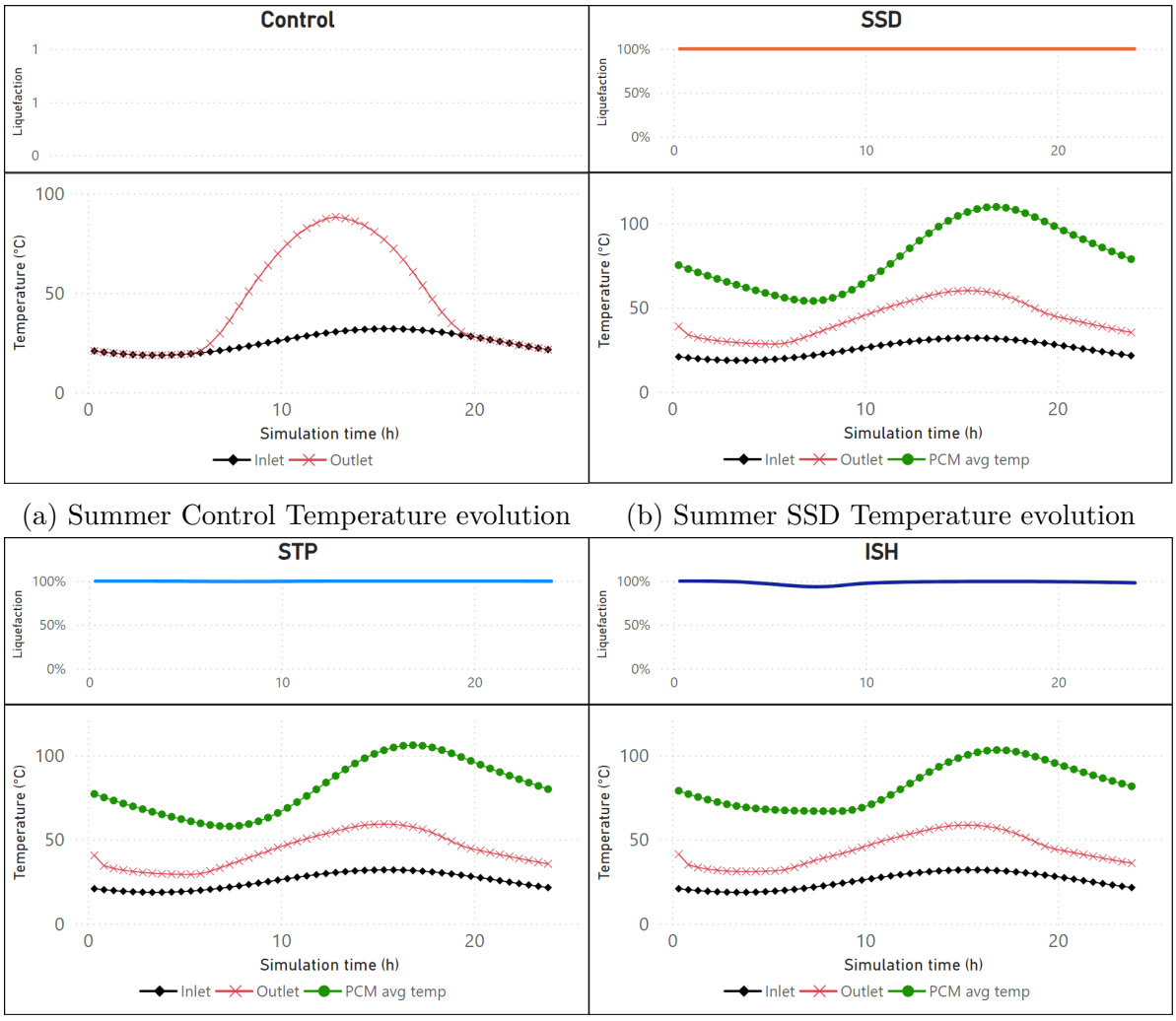

(a) Summer Control Temperature evolution

(b) Summer SSD Temperature evolution

(c) Summer STP Temperature evolution

(d) Summer ISH Temperature evolution

Figure 4.8: Simulated summer temperature evolution

constant, demonstrating temperature stability and highlighting the effectiveness of ISH in maintaining a steady average outlet temperature.

4.1.2 Winter

Following the same procedures, Figures 4.9 and 4.10 show the temperature contours for the control and SSD simulations for winter conditions.

The comparison of the temperature evolution among the three selected PCMs reveals that the simulation with the greatest temperature delta between midnight and the peak

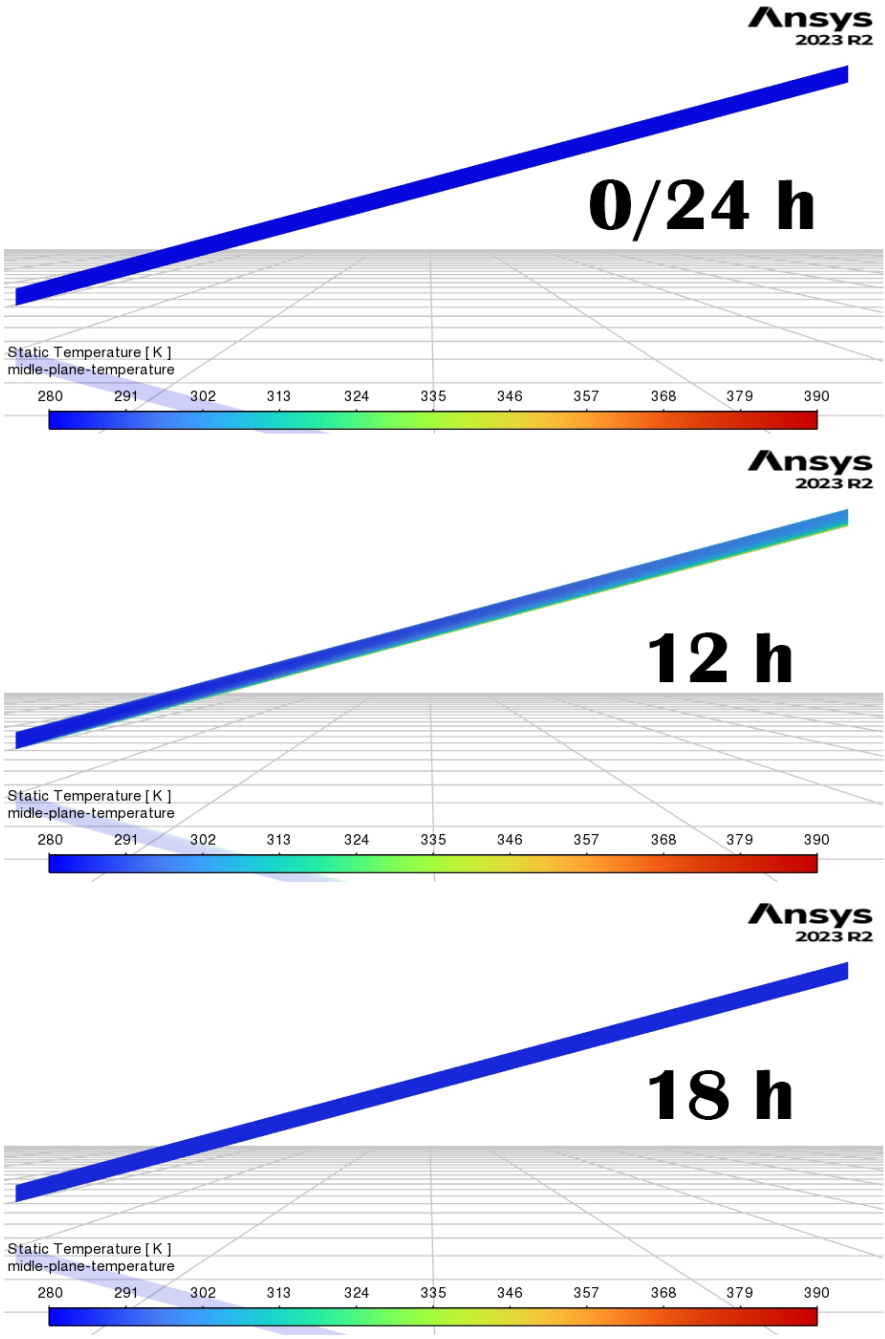

Figure 4.9: Winter Control temperature contours

daytime temperature was the control case, as shown in Figure 4.9, the same way as show in the summer control simulations results. This highlights the effect of the absence of PCM on temperature regulation, with the control case experiencing more pronounced

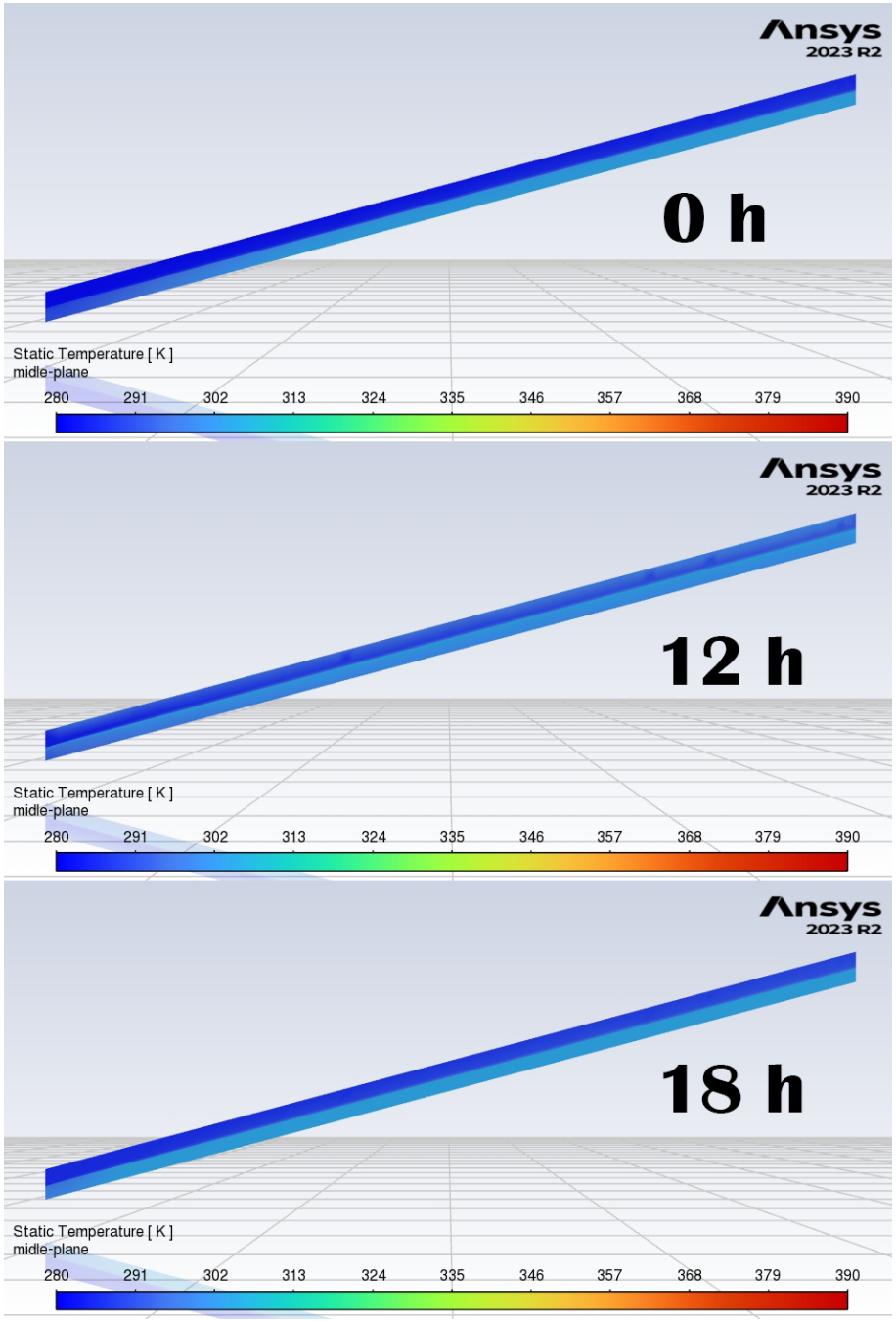

Figure 4.10: Winter SSD temperature contours

fluctuations as expected. Figure 4.10 show the temperature gain compared to Figure 4.9 where there is no TES.

Figure 4.11a illustrates the inlet temperature variation over time, following the sinusoidal pattern described in Subsection 3.2.2 the same way as shown in the summer section.

Continuing the analysis, Figure 4.11b illustrates the temperature evolution at the collector's outlet. A key observation is the more pronounced temperature fluctuations in the control system compared to those with PCM, where all three PCMs maintain a more stable outlet temperature, consistent with the results observed during the summer simulations. Among the tested materials, SSD demonstrated the most consistent temperature regulation, which can be attributed to its phase change temperature. This stability is evident in Figure 4.11b, where the temperature amplitude of the SSD system is smaller compared to STP and ISH. This comparison is further highlighted in Figure 4.11c, where the temperature amplitude is clearly visible. While all three PCMs reach the same lowest temperature, SSD does not exhibit the same rise to higher temperatures, owing to its phase change temperature, which limits excessive temperature increases.

Continuing with the analysis of temperature evolution across each simulation, Figure 4.12 illustrates the progression of inlet, outlet, and PCM temperatures, as well as the liquefaction fraction of the PCM. A detailed explanation of the graph structure and interpretation is provided in the Summer Temperature Evolution Subsection.

Analyzing Figure 4.12, it is evident that Figure 4.12a shows the largest temperature differential, which is attributed to the absence of any TES. Among the simulated PCMs, only SSD (Figure 4.12b) exhibits distinct behavior, as it is the only material undergoing phase change. During the phase change process, the outlet temperature remains relatively constant, demonstrating temperature stability and highlighting the effectiveness of SSD in maintaining a steady average outlet temperature.

4.2 Energy evaluation

This section evaluates the energy of the system, as well as the system energy output in of-sun hours.

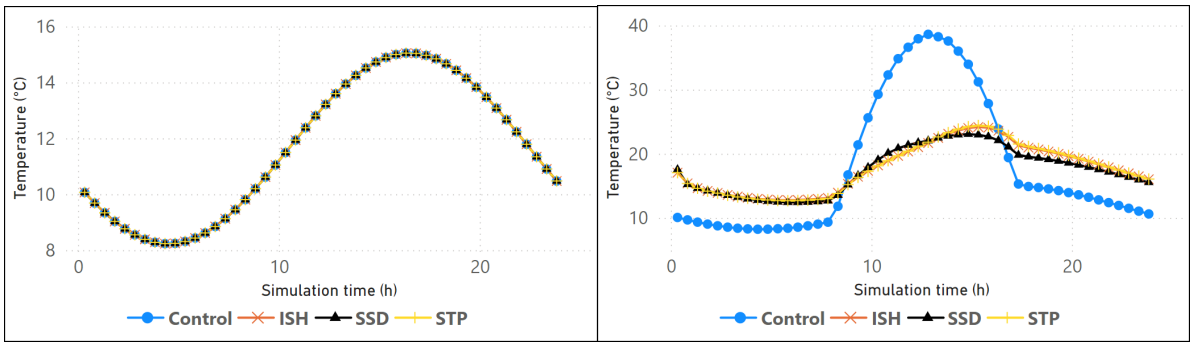

(a) Winter inlet temperature (b) Winter outlet temperature

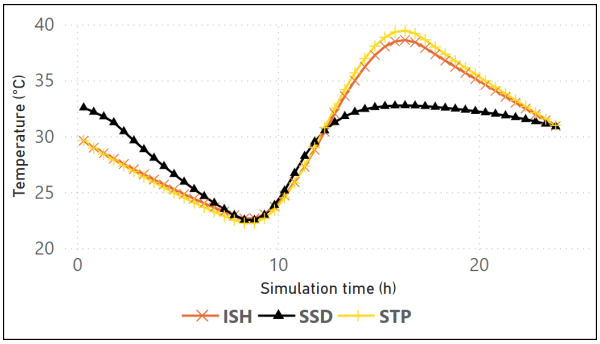

(c) Winter average PCM temp

Figure 4.11: Winter temperature profiles

Gathering the information from Subsection 3.2.1 it is possible to obtain the data shown in Table 4.1. This table show the average sun irradiance values, the simulations was conduced during December for winter and July for summer, $85,35\,W/m^2$ and $248,00\,W/m^2$ respectively, values that will be utilizes in 4.2 for comparison reasons.

Table 4.2 highlights the differences between the simulations, with the most significant observation being the comparison of average temperatures during off-sun hours between the PCM simulations and the control simulation, marked in the table as the "Delta off-sun hours (°C)" row. For the PCM simulations under summer conditions, the temperature difference between inlet and outlet remains between 12 and 14 degrees, whereas in the control simulation, the difference is practically zero.

Under winter conditions, the average temperature variation ranges between 4 and 6 degrees for the PCM simulations, while the control simulation continues to show nearly zero variation during off-sun hours. This demonstrates the PCMs' capacity to store and

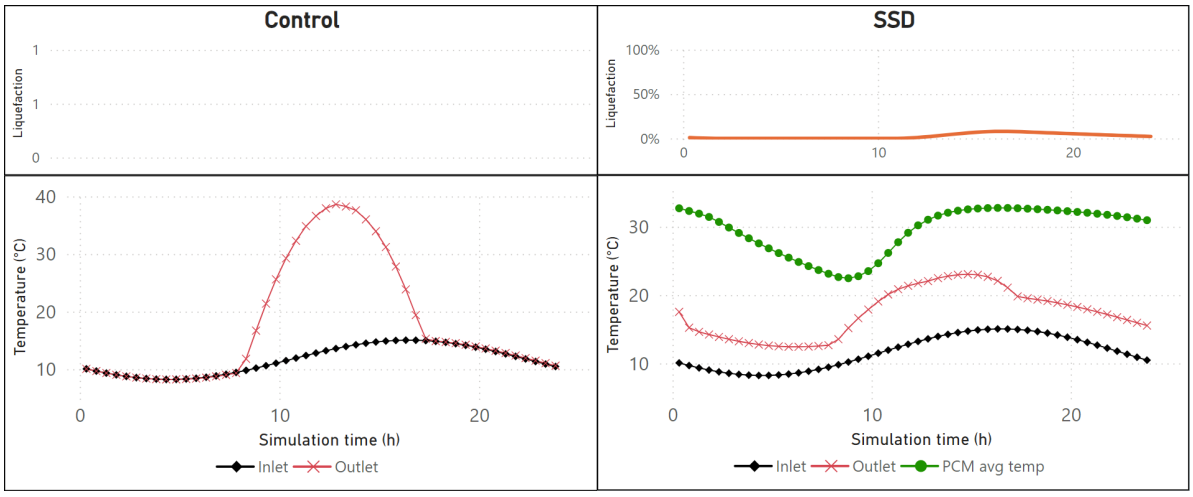

(a) Winter Control Temperature evolution

(b) Winter SSD Temperature evolution

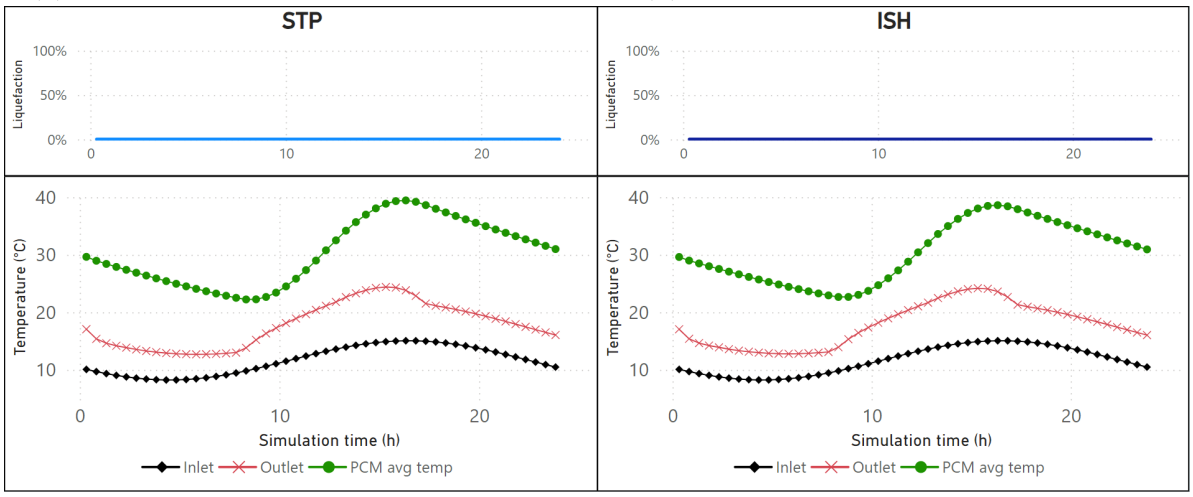

(c) Winter STP Temperature evolution

(d) Winter ISH Temperature evolution

Figure 4.12: Simulated winter temperature evolution

release heat, maintaining a more consistent temperature in the system compared to the control.

Figures 4.13a and 4.13b provide a graphical representation of the system's output energy in W/m^2 and the temperature gain from the inlet to the outlet.

Given that the system operates under stable conditions, the energy entering the system should approximately match the energy exiting it. Therefore, the average output energy should align closely with the "Hourly Average (W/m^2)" values in Table 4.1. For the winter simulations, December data were used, while July data were employed for the summer

Table 4.1: Available energy per month

	Day Energy (W/m^2)	Hourly Average (W/m^2)
Jan	2162,26	90,09
Feb	2713,54	113,06
Mar	3165,34	131,89
Apr	3661,76	152,57
May	4425,49	184,40
Jun	5019,66	209,15
Jul	5952,01	248,00
Aug	5537,52	230,73
Sep	4285,36	178,56
Oct	2967,45	123,64
Nov	2208,26	92,01
Dec	2048,37	85,35

Table 4.2: Energy and temperature simulation results

		Control	SSD	ISH	STP
Summer	Output energy (W/m^2)	242,96	231,39	237,61	232,65
	Solar irradiance (W/m^2)	248,00	248,00	248,00	248,00
	Delta off-sun hours (°C)	0,02	12,54	13,94	13,10
Winter	Output energy (W/m^2)	81,22	74,73	79,54	80,05
	Solar irradiance (W/m^2)	85,35	85,35	85,35	85,35
	Delta off-sun hours (°C)	0,05	4,86	5,32	5,33

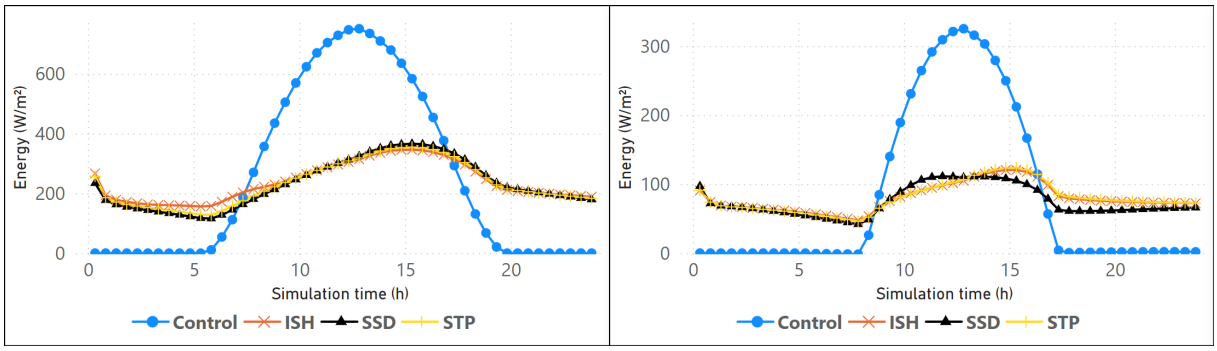

(a) Summer output energy

(b) Winter output energy

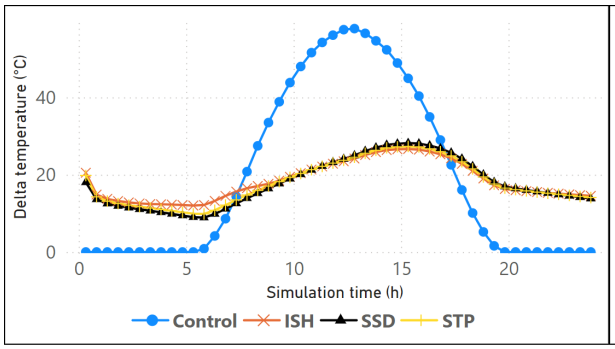

(c) Summer Temperature difference

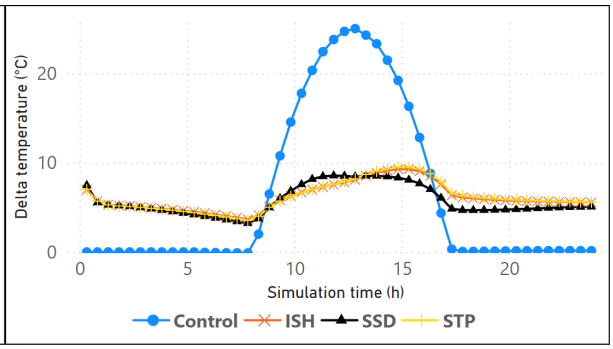

(d) Winter Temperature difference

Figure 4.13: System evaluation

simulations, as these months represent the periods of highest and lowest solar irradiance throughout the year.

A slight deviation is observed comparing solar irradiance and energy output in Table 4.2 due to several factors. Despite the correction applied to the direct solar irradiance, as discussed in Subsection 3.2.1, discrepancies remain between the solar irradiance data from PVGIS and the values calculated by the ANSYS solar calculator. Additionally, the system stabilization criteria outlined in Subsection 3.4.2 accept some differences between the initial and final energy levels during the simulation, further contributing to the variations shown in Table 4.1.

Analyzing Figures 4.13a and 4.13b, it is evident that the system's energy outputs demonstrate stability compared to the control, both in summer and winter conditions. These figures corroborate the findings from the temperature analysis, where the ISH PCM exhibited the most stable performance during summer, while SSD PCM showed

the most consistent energy output during winter. Figures 4.13c and 4.13d show the reflected behavior, where the delta temperature between the input and outlet shows a clear stabilization from the control to the PCM based systems.

4.3 PCM liquefaction evaluation

This section details the PCMs phase change evolution and analysis for summer and winter simulations. To highlight the phase change differences between the seasons, the scale used in the images was maintained consistently across both.

4.3.1 Summer

Figures 4.14, and 4.15 illustrate the evolution of material liquefaction and solidification throughout the simulation. It is evident that both SSD and STP do not exhibit any solidification during the summer simulation, indicating that the utilization of these materials in summer conditions is comparable to using inert substances, such as rocks, which do not undergo a phase change. Conversely, Figure 4.15 demonstrates the initiation of the solidification process for the ISH PCM, highlighting its unique behavior relative to the other materials during the summer simulation, such as SSD and STP.

Continuing with the phase change analysis, Figure 4.16a presents a comparison of the three simulated materials. As discussed in Section 4.1, the only material that undergoes the solidification process under summer conditions is the ISH.

4.3.2 Winter

Continuing the evaluation from the summer analysis, it is clear that both STP and ISH do not exhibit any liquefaction during the winter simulation, as show in Figure 4.18, indicating that their utilization under winter conditions is similar to using inert materials. In contrast, Figure 4.17, at 18h, shows the liquefaction process for the SSD PCM. The liquefaction begins as expected, at the top of the collector and adjacent to the collector

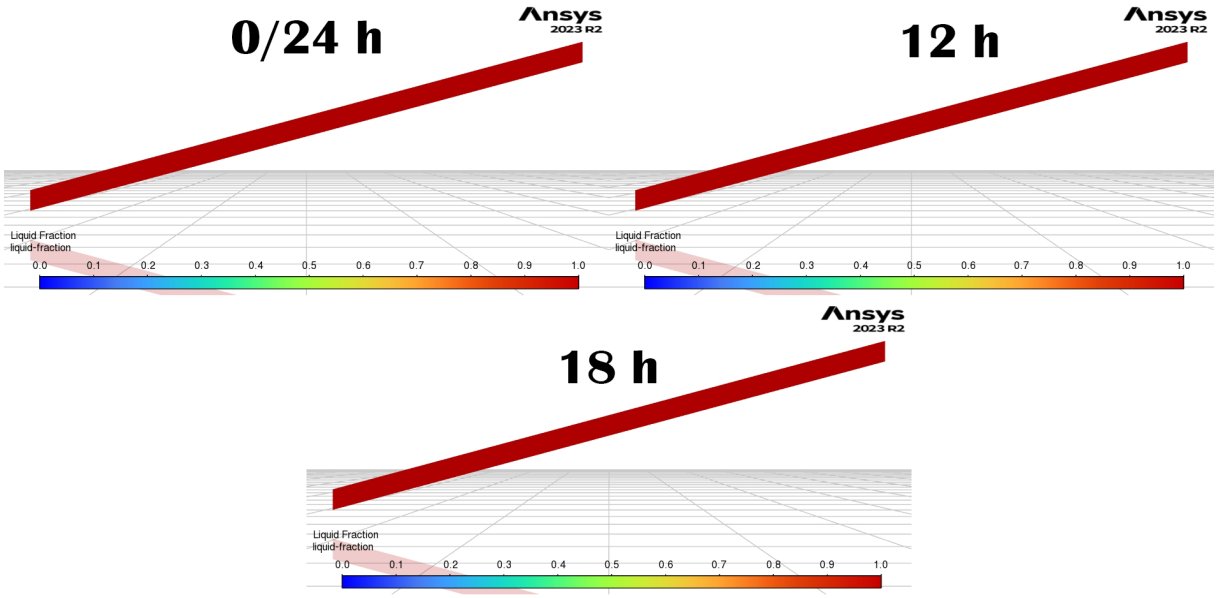

Figure 4.14: Summer STP and SSD Liquefaction rate

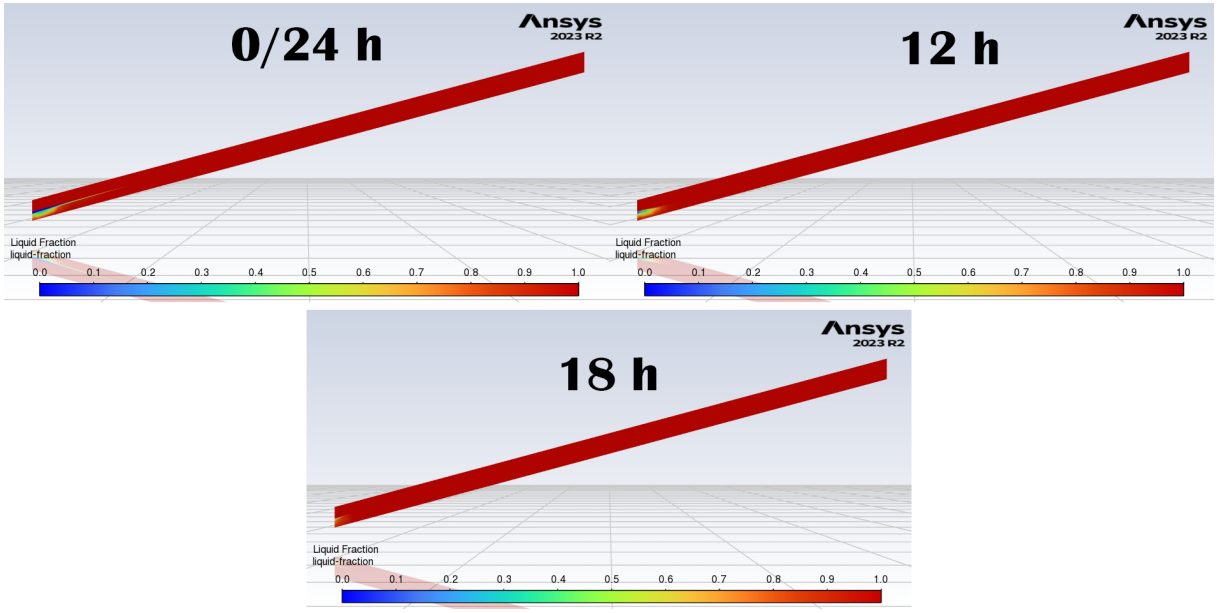

Figure 4.15: Summer ISH Liquefaction rate

plate, area responsible to collect solar radiation and transfer it to the PCM encapsulation and transfer the heat to the air passing above (in red on Figure 4.18 and 4.17) reason for the PCM heating and responsible for the phase change behavior, demonstrating the accurate representation of real-world behavior within the simulation. This consistency

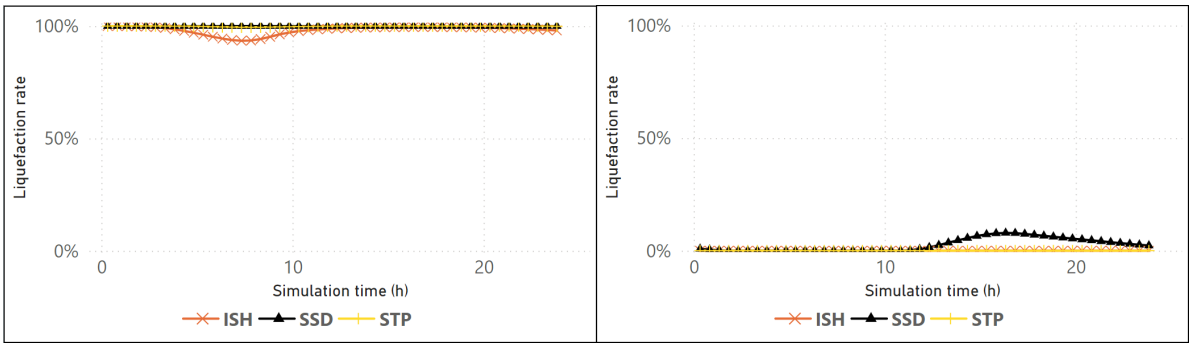

(a) Summer PCMs liquefaction rate (b) Winter PCMs liquefaction rate

Figure 4.16: System liquefaction rate

further validates the simulation setup and boundary conditions.

This behavior is expected due to the proximity of the collector plate to the PCM and the plate's high thermal conductivity, as it transfers thermal energy both to the air passing above and the PCM below. Another anticipated outcome is that the liquefaction process is more pronounced in the top part of the collector. This occurs because the temperature of the incoming air prevents the bottom part of the PCM from liquefying at the same rate as the top.

Continuing with the phase change analysis, Figure 4.16b presents a comparison of the three simulated materials. As discussed in Section 4.1, the only material that undergoes the liquefaction process under winter conditions is the SSD.

4.4 Discussions

Starting with the material amount definition derived from Equation 3.6, the simulation results and the melting/solidification gradients shown in Figures 4.15, 4.18, 4.17 and 4.18 provide a reasonable representation of the expected behavior. However, the total daily energy used to calculate the necessary material amount should ideally be based on direct solar radiation. In this work, global radiation was utilized, which resulted in less optimal phase change transitions due to the larger thermal mass of the PCM storage. Consequently, this influenced the effectiveness of the phase-change process of the material

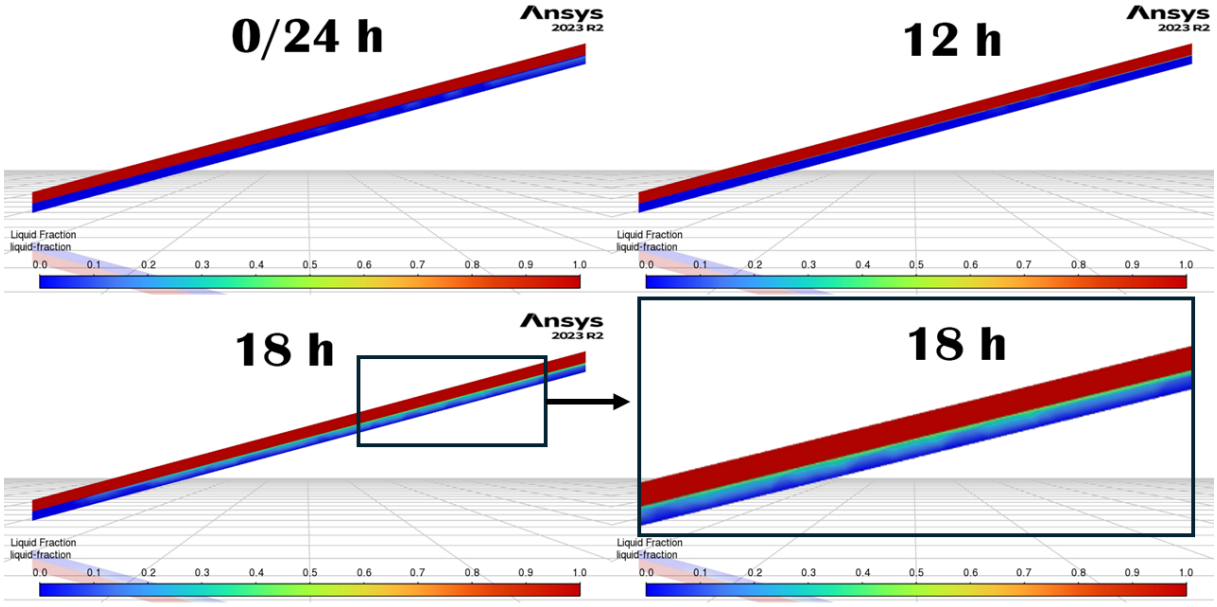

Figure 4.17: Winter SSD Liquefaction rate

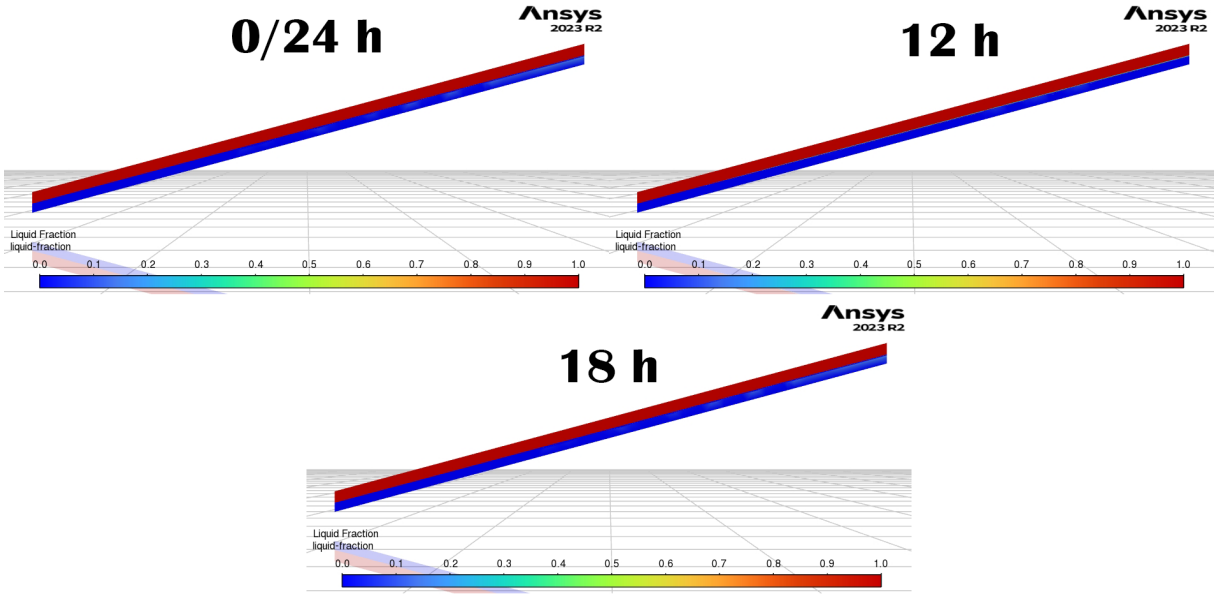

Figure 4.18: Winter STP and ISH Liquefaction rate

as less material should lead to a grater thermal variation implying more phase change occur. Less material imply in lower PCM thickness, meaning the energy stored in the PCM flows faster to the air.

Although the simulation demonstrated a small phase change in the ISH simulation in summer conditions, as shown in Figure 4.8d, it did not account for environmental energy losses, construction variances, or heat dissipation due to imperfect insulation of the PCM walls. Consequently, the amount of material undergoing phase change in real-world conditions would likely be greater. To substantiate this hypothesis, it would be necessary to construct a test collector with identical parameters and conduct experimental trials to further validate the simulation results. Nonetheless, the ISH PCM appears highly suitable for summer applications, given its high phase change temperature (64°C), significant thermal capacity (200 kJ/kg), and low cost (17,38 €/m²). It offers an economically viable solution for summer TES in STB applications.

Although the simulation demonstrated a small phase change in the SSD simulation under winter conditions, as shown in Figure 4.12b, it did not account for energy losses. As a result, the amount of material undergoing phase change in real-world scenarios would likely be lower. To validate this hypothesis, constructing a test collector with identical parameters and conducting experimental trials would be necessary. Nevertheless, SSD PCM appears less suitable for winter applications, as a material with a lower melting temperature would be more appropriate for peak winter conditions. However, for transitional months such as October or March, SSD could meet the requirements, given its low cost (5,2 €/m²) and high latent heat of fusion (245 kJ/kg), making it an economical choice for thermal energy storage.

Referring to Figure 4.4, it is evident that the airflow first absorbs thermal energy from the bottom of the collector and later from the top. This indicates that the bottom section of the PCM storage will never melt before the top, thereby preventing potential convection issues within the TES. This sequential energy transfer ensures more uniform melting and temperature distribution across the TES.

Regarding energy storage and release during off-sun hours, Figures 4.13a, 4.13b, 4.13c and 4.13d illustrate the system's behavior during these periods. It is evident that the proposed solution maintains a stable rate of thermal energy transfer between the PCM

and the air, allowing the system downstream of the collector's air outlet to continue operating even in the absence of sunlight. This capability significantly extends the system's operational time, possibly enhancing overall system efficiency.

Referring to the fourth item in Section 3.2.3 "Durability Against Solidification/Melting Cycles", specifically regarding the SSD PCM, this material exhibits vulnerability to a loss in latent heat of fusion due to an elevated number of solidification/melting cycles, as highlighted by [22]. To mitigate this issue, [22] proposed a variety of solutions to reduce this degradation. Additionally, with respect to the material's supercooling behavior, this factor was not incorporated into the simulations. However, as also noted by [22], SSD has a supercooling temperature of approximately $8°C$. For the conducted simulations, this supercooling phenomenon would not present a significant issue since the material never fully melted. Therefore, a sufficient amount of solid phase would remain, allowing for the nucleation of the solidification process in adjacent regions during winter conditions.

Chapter 5

Conclusion

The objective of this master's thesis was to develop an affordable thermal energy storage (TES) system using phase change materials (PCM) for application in solar thermal collectors to heat air. This objective was successfully achieved. However, certain aspects could be further refined to enhance the study's outcomes. One such improvement would be adjusting the slope of the collector plane; a 15° slope was used, but the optimal year-round slope for the selected region is 30.8°. Additionally, simulating a material with a higher melting temperature, in the range of 70 to 75°C, could provide valuable insights. Finally, reducing the time step from 600 seconds to 60 seconds would likely increase the accuracy of the simulations, leading to more accurate results.

The presented correction method for the ANSYS solar calculator performed as expected. However, this correction should not have been necessary when comparing the discrete PVGIS data with the solar calculator data, as the simulation software should inherently provide the correct amount of direct irradiation. In winter conditions, without the applied correction factor, the direct irradiation reaching the collector would have been nearly three times higher than the actual value. For the summer scenario, while the discrepancy is less pronounced, there remains a 40% difference between the expected and solar calculator values, which represents 2,38 kW/m^2 for each simulation day.

This master's thesis successfully achieved its goal of developing and simulating an affordable thermal energy storage (TES) system using PCM for application in solar thermal

collectors to heat air. The simulations provided valuable insights into the performance of different PCMs under both summer and winter conditions. However, certain limitations, such as the exclusion of environmental energy losses and variances in real-world construction, suggest that further experimental validation is necessary to refine the findings. For the development of the TES system for summer applications, the ISH PCM demonstrated the most favorable results, requiring 112 kg of material at a cost of €17,38. This configuration achieved a stable temperature differential of 13,1°C between the collector's inlet and outlet during off-sun hours. For winter applications, while SSD did not yield optimal results, it performed effectively, requiring only 90 kg of material to store the necessary energy at a cost of €5,42, making it the most economical solution. Under winter conditions, SSD maintained a temperature differential of 4,84°C between inlet and outlet during off-sun hours.

The study also demonstrated that ISH PCM is particularly effective for summer applications, while SSD PCM shows potential for transitional months but may not be optimal for peak winter conditions. Additionally, the stability of the system's thermal energy transfer during off-sun hours further underscores the viability of PCM-based TES systems for extending operational time. Overall, while the proposed solution shows promise, future research should focus on experimental validation and explore additional configurations to optimize performance.

Bibliography

[1] H. Lucatero, L. Romero-Salazar, E. Ruiz, M. Mayorga, and J. Arteaga-Arcos, "Solar dryer exergetic and energetic efficiency analysis," in *Proceedings of COMSOL conference Boston*, 2015.

[2] A. Lingayat, V. Chandramohan, and V. Raju, "Design, development and performance of indirect type solar dryer for banana drying," *Energy Procedia*, vol. 109, pp. 409–416, 2017.

[3] P. D. Tegenaw, M. G. Gebrehiwot, and M. Vanierschot, "Design and cfd modeling of a solar food drier," in *EuroDrying'2017, Date: 2017/06/19-2017/06/21, Location: Liége, Belgium*, 2017, pp. 183–184.

[4] Y. Amanlou and A. Zomorodian, "Applying cfd for designing a new fruit cabinet dryer," *Journal of food engineering*, vol. 101, no. 1, pp. 8–15, 2010.

[5] E. Torres-Reyes, J. Navarrete-Gonzalez, and B. Ibarra-Salazar, "Thermodynamic method for designing dryers operated by flat-plate solar collectors," *Renewable energy*, vol. 26, no. 4, pp. 649–660, 2002.

[6] P. Demissie, M. Hayelom, A. Kassaye, A. Hailesilassie, M. Gebrehiwot, and M. Vanierschot, "Design, development and cfd modeling of indirect solar food dryer," *Energy Procedia*, vol. 158, pp. 1128–1134, 2019.

[7] J. K. Andharia, B. Markam, D. Dzhonova, and S. Maiti, "A comparative performance analysis of sensible and latent heat based storage in a small-scale solar thermal dryer," *Journal of Energy Storage*, vol. 45, p. 103 764, 2022.

[8] A. El Khadraoui, S. Bouadila, S. Kooli, A. Farhat, and A. Guizani, "Thermal behavior of indirect solar dryer: Nocturnal usage of solar air collector with pcm," *Journal of cleaner production*, vol. 148, pp. 37–48, 2017.

[9] C. Suresh and R. P. Saini, "Thermal performance of sensible and latent heat thermal energy storage systems," *International Journal of Energy Research*, vol. 44, no. 6, pp. 4743–4758, 2020.

[10] A. Reyes, A. Mahn, and F. Vásquez, "Mushrooms dehydration in a hybrid-solar dryer, using a phase change material," *Energy Conversion and management*, vol. 83, pp. 241–248, 2014.

[11] D. Jain and P. Tewari, "Performance of indirect through pass natural convective solar crop dryer with phase change thermal energy storage," *Renewable energy*, vol. 80, pp. 244–250, 2015.

[12] A. Bhardwaj, R. Chauhan, R. Kumar, M. Sethi, and A. Rana, "Experimental investigation of an indirect solar dryer integrated with phase change material for drying valeriana jatamansi (medicinal herb)," *Case studies in thermal engineering*, vol. 10, pp. 302–314, 2017.

[13] S. Shalaby and M. Bek, "Experimental investigation of a novel indirect solar dryer implementing pcm as energy storage medium," *Energy conversion and management*, vol. 83, pp. 1–8, 2014.

[14] V. M. Swami, A. T. Autee, and T. Anil, "Experimental analysis of solar fish dryer using phase change material," *Journal of Energy Storage*, vol. 20, pp. 310–315, 2018.

[15] W. B. Chaouch, A. Khellaf, A. Mediani, M. E. A. Slimani, A. Loumani, and A. Hamid, "Experimental investigation of an active direct and indirect solar dryer with sensible heat storage for camel meat drying in saharan environment," *Solar Energy*, vol. 174, pp. 328–341, 2018.

[16] H. Atalay, "Performance analysis of a solar dryer integrated with the packed bed thermal energy storage (tes) system," *Energy*, vol. 172, pp. 1037–1052, 2019.

[17] T. Khadiran, M. Z. Hussein, Z. Zainal, and R. Rusli, "Advanced energy storage materials for building applications and their thermal performance characterization: A review," *Renewable and Sustainable energy reviews*, vol. 57, pp. 916–928, 2016.

[18] A. Sharma, V. V. Tyagi, C. R. Chen, and D. Buddhi, "Review on thermal energy storage with phase change materials and applications," *Renewable and Sustainable energy reviews*, vol. 13, no. 2, pp. 318–345, 2009.

[19] A. Pasupathy, R. Velraj, and R. Seeniraj, "Phase change material-based building architecture for thermal management in residential and commercial establishments," *Renewable and Sustainable Energy Reviews*, vol. 12, no. 1, pp. 39–64, 2008.

[20] I. Dincer, "On thermal energy storage systems and applications in buildings," *Energy and buildings*, vol. 34, no. 4, pp. 377–388, 2002.

[21] S. D. Sharma and K. Sagara, "Latent heat storage materials and systems: A review," *International journal of green energy*, vol. 2, no. 1, pp. 1–56, 2005.

[22] J. R. Hirschey, N. Kumar, T. Turnaoglu, K. R. Gluesenkamp, and S. Graham, "Review of low-cost organic and inorganic phase change materials with phase change temperature between 0° c and 65° c," 2021.

[23] H. P. Garg, S. C. Mullick, and V. K. Bhargava, *Solar thermal energy storage*. Springer Science & Business Media, 2012.

[24] S. Hasnain, "Review on sustainable thermal energy storage technologies, part i: Heat storage materials and techniques," *Energy conversion and management*, vol. 39, no. 11, pp. 1127–1138, 1998.

[25] D. Buddhi and R. Sawhney, "Proc: Thermal energy storage and energy conversion," *School of Energy and Environmental Studies, Devi Ahilya University, Indore, India*, 1994.

[26] D. Hale, M. Hoover, and M. ONeill, "Phase change materials handbook. report no," NASA-CR-61363. Contract no.: NAS8-25183. NASA, Tech. Rep., 1971.

[27] G. A. Lane and G. Lane, *Solar heat storage: latent heat materials*. CRC press Boca Raton, FL, USA: 1983, vol. 1.

[28] A. Abhat, "Low temperature latent heat thermal energy storage: Heat storage materials," *Solar energy*, vol. 30, no. 4, pp. 313–332, 1983.

[29] A. Sharma, S. Sharma, and D. Buddhi, "Accelerated thermal cycle test of acetamide, stearic acid and paraffin wax for solar thermal latent heat storage applications," *Energy Conversion and Management*, vol. 43, no. 14, pp. 1923–1930, 2002.

[30] A. S. Fleischer, *Thermal energy storage using phase change materials: fundamentals and applications*. Springer, 2015.

[31] N. Xie, Z. Huang, Z. Luo, X. Gao, Y. Fang, and Z. Zhang, "Inorganic salt hydrate for thermal energy storage," *Applied Sciences*, vol. 7, no. 12, p. 1317, 2017.

[32] M. I. Lone and R. Jilte, "A review on phase change materials for different applications," *Materials Today: Proceedings*, vol. 46, pp. 10 980–10 986, 2021.

[33] V. Alexiades, A. Solomon, and D. Wilson, "The formation of a solid nucleus in supercooled liquid, i," 1988.

[34] E. P. Ona, X. Zhang, K. Kyaw, *et al.*, "Relaxation of supercooling of erythritol for latent heat storage," *Journal of chemical engineering of Japan*, vol. 34, no. 3, pp. 376–382, 2001.

[35] M. M. Farid, A. M. Khudhair, S. A. K. Razack, and S. Al-Hallaj, "A review on phase change energy storage: Materials and applications," *Energy conversion and management*, vol. 45, no. 9-10, pp. 1597–1615, 2004.

[36] S. Hirano and T. S. Saitoh, "Heat balance of long-term supercooled thermal energy storage," in *IECEC- 36 th Intersociety Energy Conversion Engineering Conference*, 2001, pp. 701–706.

[37] S. Hirano and T. S. Saitoh, "Influence of operating temperature on efficiency of supercooled thermal energy storage," in *IECEC'02. 2002 37th Intersociety Energy Conversion Engineering Conference, 2002.*, IEEE, 2002, pp. 684–689.

[38] P. Barrett and B. Best, "Thermal energy storage in supercooled salt mixtures," *Materials chemistry and physics*, vol. 12, no. 6, pp. 529–536, 1985.

[39] M. H. Zahir, S. A. Mohamed, R. Saidur, and F. A. Al-Sulaiman, "Supercooling of phase-change materials and the techniques used to mitigate the phenomenon," *Applied energy*, vol. 240, pp. 793–817, 2019.

[40] A. Safari, R. Saidur, F. Sulaiman, Y. Xu, and J. Dong, "A review on supercooling of phase change materials in thermal energy storage systems," *Renewable and Sustainable Energy Reviews*, vol. 70, pp. 905–919, 2017.

[41] B. Sandnes and J. Rekstad, "Supercooling salt hydrates: Stored enthalpy as a function of temperature," *Solar energy*, vol. 80, no. 5, pp. 616–625, 2006.

[42] D. Colvin and G. Bryant, "Advances in heat and mass transfer in biotechnology," *ASME HTD*, vol. 44, p. 199, 1999.

[43] G. A. Lane, "Low temperature heat storage with phase change materials," *International Journal of Ambient Energy*, vol. 1, no. 3, pp. 155–168, 1980.

[44] E. E.
bibinitperiod R. Energy. "Solar radiation basics." (2024), [Online]. Available: `https://www.energy.gov/eere/solar/solar-radiation-basics` (visited on 09/23/2024).

[45] T. O. Kvålseth, "Cautionary note about r 2," *The American Statistician*, vol. 39, no. 4, pp. 279–285, 1985.

[46] T. Chen, H. Sun, P. Mu, *et al.*, "Fatty amines as a new family of organic phase change materials with exceptionally high energy density," *Solar Energy Materials and Solar Cells*, vol. 206, p. 110 340, 2020.

[47] A. El Khadraoui, S. Bouadila, S. Kooli, A. Guizani, and A. Farhat, "Solar air heater with phase change material: An energy analysis and a comparative study," *Applied Thermal Engineering*, vol. 107, pp. 1057–1064, 2016.

[48] R. E. Parkin, "A note on the extinction coefficient and absorptivity of glass," *Solar Energy*, vol. 114, pp. 196–197, 2015.

[49] P. Rani and P. Tripathy, “Cfd coupled heat and mass transfer simulation of pineapple drying process using mixed-mode solar dryers integrated with flat plate and finned collector,” *Renewable Energy*, vol. 217, p. 119 210, 2023.